https://doi.org/10.1016/j.autcon.2023.105130

Corrosion Assessment Using Ground Penetrating Radar in Reinforced Concrete Structures: Influential Factors and Analysis Methods

Nour Faris[1], Tarek Zayed[1], Eslam Mohammed Abdelkader[1,2], Ali Fares[1*].

[1] Department of Building and Real Estate, Faculty of Construction and Environment, The Hong Kong Polytechnic University, Kowloon 999077, Hong Kong

[2] Structural Engineering Department, Faculty of Engineering, Cairo University, Giza 12613, Egypt
Correspondence: eslam.abdelkader@polyu.edu.hk

Abstract

Reinforcement corrosion is a common cause of damage in concrete structures, resulting in cracking and spalling of the surrounding concrete. Recently, ground penetrating radar (GPR) has become the primary non-destructive testing (NDT) for examining the corrosiveness of concrete structures. However, the analysis of GPR data can be intricate and time-consuming due to a range of factors affecting GPR waves. To this end, this paper presents a systematic review of influential factors and analysis methods for GPR-based corrosion assessment in concrete structures. The review analysis found that corrosion boosts the reflected waves' amplitude by propagating rust into concrete cracks, while the simultaneous presence of chloride and moisture severely attenuates the amplitude and frequency of electromagnetic waves. In addition, B-scans analysis is more thorough but also subjective and time-consuming and lacks for comprehensive methodology to automate its process. Thereafter, this study offers insights for improving the efficiency of GPR-based corrosion assessment.

Keywords: Ground penetrating radar, Corrosion, Factors, Bridge deck, NDT, Analysis methods, Concrete structures, Infrastructure, Systematic review.

1 Introduction

Reinforced concrete is a vital component of civil infrastructure systems [1]. Maintaining the concrete condition within sufficient functional and safety levels is an important mandate for the relevant authorities [2] . Concrete bridges are among the most commonly encountered forms of concrete infrastructure. For instance, there are more than 617,000 concrete bridges across the United States, and currently, 42% of these bridges are more than 50 years old, with more than 46,154 bridges reported to be structurally deficient [3]. Similarly, according to a recent Canadian infrastructure report (2019), almost 40% of the Canadian concrete bridges were either in Very Poor, Poor, or Fair condition, which is a substantial increase when compared to nearly 26% in 2016 [4]. In addition to concrete bridges, other concrete structures such as tunnels, concrete slabs, retaining walls, and foundations are commonly subjected to ongoing deterioration. To this end, efficacious condition assessment is entailed to monitor the structural integrity and deterioration rates of concrete structures, which paves the way for informed financial decisions regarding the allocation of maintenance resources.

Various mechanical, physical, and chemical factors can deteriorate concrete structures. The encountered deterioration rate varies according to the applied loads and environmental exposure [5]. The continued exposure of reinforced concrete elements accelerates the corrosion of their reinforcement [6]. Corrosion is a chemical reaction that causes the accumulation of rust on the surface of the steel rebars, which can eventually penetrate the steel and weaken its load-bearing capacity. The primary cause of steel corrosion is exposure to chloride ions, carbon dioxide, and moisture [7]. As the corrosion continues, the rusted steel expands and induces interior tensile stresses, causing cracks and spalling in the surrounding concrete [8]. Thus, regular inspection and maintenance are essential for detecting and minimizing the effect of reinforcement corrosion. In recent years, ground penetrating radar (GPR) has been acknowledged as the primary non-destructive technique (NDT) for investigating the

corrosiveness of concrete structures [9]. Infrastructure operators and managers increasingly prefer using GPR because it can yield data at high speed and high spatial resolution [10,11]. Although GPR renders a real-time electromagnetic NDT for reinforcement assessment, the analysis and interpretation of GPR data are complex and time-consuming. The complexity of these processes arises from the presence of numerous factors that exert influences on GPR waves. These factors encompass physical, environmental, chemical, and technical aspects. The lack of a comprehensive understanding of the effect of these factors induces uncertainty and bias in GPR interpretation results. Over the past decade, GPR has been under intensive research to comprehend the affecting factors and develop efficient methodologies for corrosion assessment. The existing literature about GPR-based corrosion assessment includes numerous interpretation methodologies that require a comprehensive analysis. In addition, the reported findings regarding the affecting factors exhibit a contradiction and require further investigation. To this end, this paper applies extensive scientometric and systematic reviews to summarise GPR data analysis methods and understand the combined effect of technical, environmental, and physical factors on GPR interpretation results. Finally, this research sheds light on the proposed future directions to ameliorate the efficiency of GPR interpretation in corrosion assessment.

2 RESEARCH METHODOLOGY

The methodology of the current study is illustrated in Fig. 1. The study unfolded in three consecutive stages: performing the search inquiry in the Scopus database, screening the search result, and conducting the scientometric and systematic analysis.

In the first stage, the search was conducted in the Scopus database to identify the relevant publications. Scopus is widely praised for being the largest and most comprehensive literature database [12,13]. The first step was formulating the research questions and identifying the goals

of the review. The review goal is to analyze research trends related to the utilization of GPR for inspecting concrete reinforcement to spot the research gaps and identify future research needs. Then, the search inquiry was set up after an extensive screening of the literature available on using the GPR for corrosion assessment. The inquiry was designed as "('rebar' OR 'reinforcement' OR 'reinforced concrete' OR 'corrosion') AND ('GPR' OR 'ground-penetrating radar' OR 'ground penetrating radar')." The unconstrained search returned a vast amount of literature, composing 933 pieces of publications.

In the second stage, the unconstrained research results were refined to select the most relevant articles, and snowballing was performed to identify the missed articles. The search results were restricted to only include articles published since 2000 using the English language. This refinement resulted in excluding more than two-thirds of the original research result. Then, the title and the abstract of the remaining articles were skimmed to exclude publications that were not relevant to the topic of this study. Consequently, only 134 articles were left for full-text review. During the full-text review, 36 articles were further excluded, considering the divergence of their focus. Finally, more pieces of articles were added through forward and backward snowballing to account for missing articles. The final number of articles considered in this study was 119.

The retained articles were used to perform a scientometric analysis. The scientometric analysis was performed using the Bibliometrix R package and VOSviewer to describe the research results. The analysis included the yearly publication trend, the most important institutions and authors, the countries/regions co-authorship, and the keywords.

Subsequently, a systematic analysis of the articles was conducted to identify the different directions of using GPR in corrosion assessment. The study delved into the factors affecting the collection and processing of GPR signals. Furthermore, the GPR signal interpretation

methods were also compared and evaluated. In addition, the automated methods for rebar localization were further analyzed. Moreover, the GPR-based deterioration modeling was investigated. Finally, research gaps and corresponding future research needs were outlined.

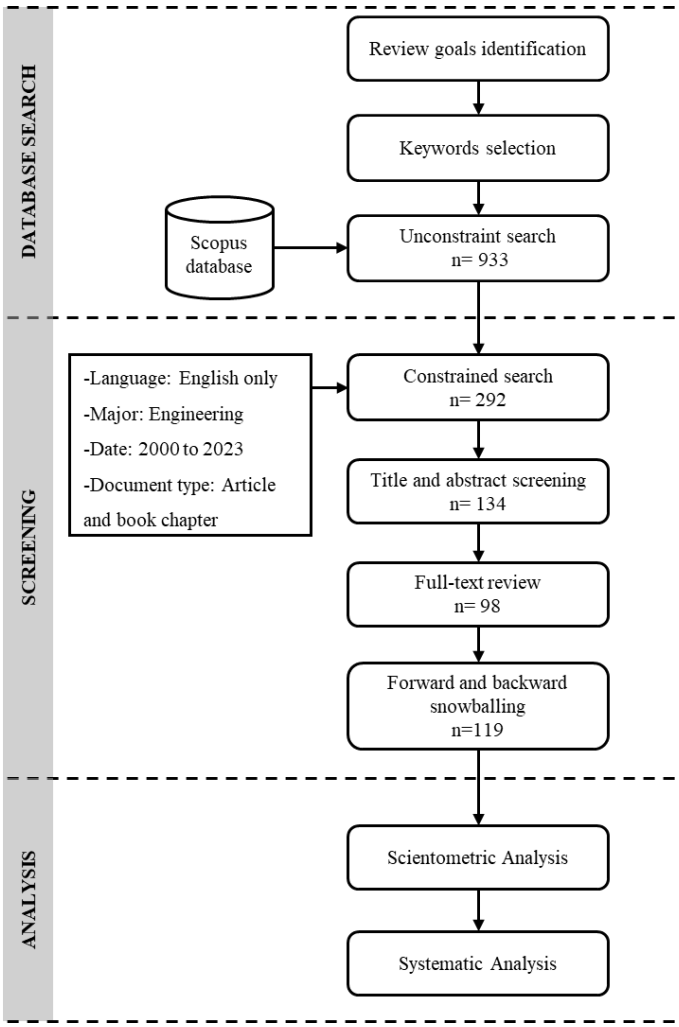

Fig. 1: Framework on the proposed research methodology.

3 SCIENTOMETRIC ANALYSIS

This study analyzed the research on using GPR for reinforcement inspection using 119 articles published since 2000. Fig. 2 shows the yearly number of publications and a moving average trend based on a two-year period. As shown in Fig. 2, limited research output in the domain of corrosion assessment in concrete structures was observed before 2012. During this period, researchers extensively delved into the application of GPR for concrete scanning to locate

embedded objects. Conversely, relatively limited attention from researchers and manufacturers has been directed toward harnessing GPR systems for corrosion assessment within expansive concrete areas such as bridge decks [14]. This can be attributed to the fuzziness of the relationship between the electromagnetic response of a reinforced concrete deck and the state of deck deterioration [15]. Recently, with the development of modern GPR systems capable of delivering finely detailed imaging and precise depth measurements, the use of GPR for detecting corrosion in concrete bridge decks has been standardized in ASTM D6087-08 standard [16,17]. However, as highlighted by Tarussov et al. [14], this standard did not consistently yield acceptable results. In response, the ASTM standard [18], revised in 2010, has transformed the GPR condition assessment from a recommended practice to a universally applicable specification. This standard delineated the procedures for conducting GPR testing and offered comprehensive guidance on data processing methodologies. This has significantly expanded the research horizons and spurred more publications to enhance the accuracy of GPR-based corrosion assessment in concrete structures. Indeed, the yearly research output increased to reach 14 and 16 in 2017 and 2022, respectively.

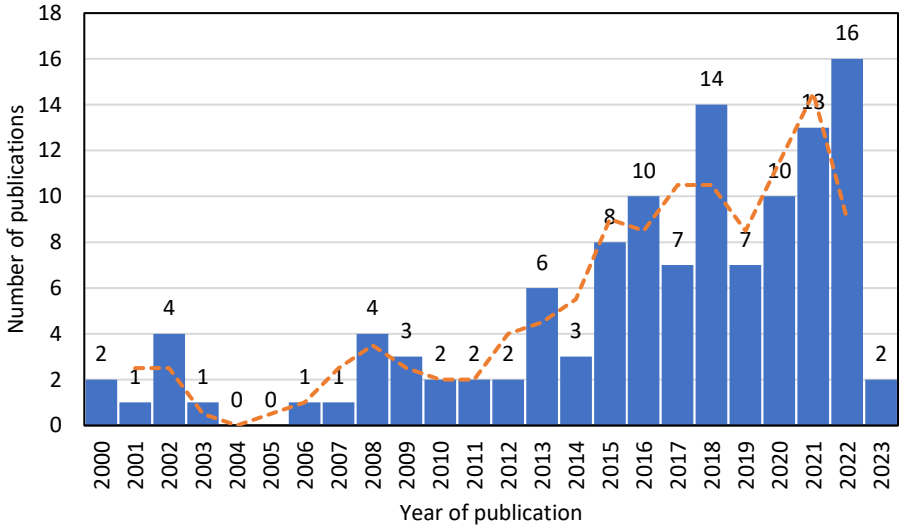

Fig. 2: Publication trend spanning over the period 2000-2023.

3.1 Countries/Regions Co-authorship Analysis

Fig. 3 elucidates the countries'/region co-authorship network in the research on corrosion assessment using GPR (CA_GPR). The scientometric analysis of countries is addressed by specifying thresholds for the minimum number of published papers and the minimum number of citations as one and zero, respectively. Consequently, it is observed that the United States of America maintains the most formidable collaboration network with a total link strength of 31. Its highest academic relationship is with Canada (link strength = 10) and China (link strength = 8). A more in-depth description of the most influential countries contributing to the CA_GPR research is given in Fig. 3. It is noted that the United States of America, China, Canada, the United Kingdom, and France are the most prolific five countries in the CA_GPR, with published documents of 52, 21, 17, 9, and 6, respectively. This signifies that this area of research is soaring in high-income countries. High-income countries are typically classified based on their Gross National Income (GNI) per capita. The classification thresholds are determined by international organizations such as the World Bank [19]. High-income countries are renowned for their robust infrastructure, leadership in technological innovation, and substantial investments in research and development [19].

The conducted analysis also expounded that the top cited affiliated countries /regions are the United States of America (1260), Canada (578), the United Kingdom (514), China (489), and Italy (358). In addition, the Netherlands (3.12), Switzerland (1.97), China (1.66), Italy (1.51), and Taiwan (1.5) are found to be the major influentials concerning average normalized citations. The average normalized citation, which can be calculated using Eq (1), allows for a relative comparison with the global average of citations received by publications of similar document types [20].

125

$$\overline{C_j} = \frac{1}{P}\sum_{i=1}^{P}\frac{C_i}{\mu_j} \quad (1)$$

126 *Ci* is the number of citations to publication *i*, *μj* is the average number of citations to
127 publications of the same type published the same year and in the same journal as article *i*, and
128 *P* is the unit's number of publications.

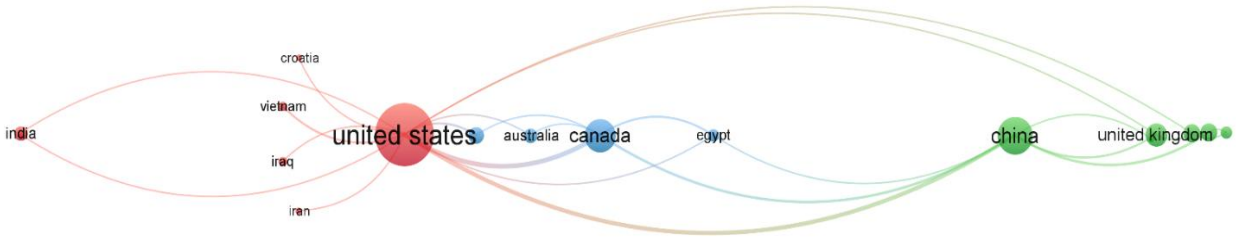

129

130 Fig. 3: Collaboration network of countries/regions working on CA_GPR research

131 Table 1: Quantitative summary of prominent countries in CA_GPR domain with respect to
132 publication count, total citations, and average normalized citations

Rank	Country/Region	Number of documents	Total citations	Normalized citations	Average publication year	Average citations	Average norm citations	Total link strength
Publication count								
1	United States of America	52	1260	54.42	2017.42	24.23	1.05	31
2	China	21	489	34.86	2018.9	23.29	1.66	18
3	Canada	17	578	18.78	2014.76	34	1.1	17
4	United Kingdom	9	514	13.23	2010.11	57.11	1.47	6
5	France	6	298	6.61	2011.83	49.67	1.10	0
Total citations								
1	United States of America	52	1260	54.42	2017.42	24.23	1.05	31
2	Canada	17	578	18.78	2014.76	34	1.1	17
3	United Kingdom	9	514	13.23	2010.11	57.11	1.47	6
4	China	21	489	34.86	2018.9	23.29	1.66	18
5	Italy	6	358	9.05	2013	59.67	1.51	4
Average normalized citations								

1	Netherlands	1	8	3.12	2022.00	8.00	3.12	2
2	Switzerland	3	225	5.92	2008.33	75	1.97	2
3	China	21	489	34.86	2018.9	23.29	1.66	18
4	Italy	6	358	9.05	2013	59.67	1.51	4
5	Taiwan	2	109	3	2015.5	54.5	1.5	0

133

3.2 Leading Institutions and Authors

The conducted bibliometric analysis exemplifies that Guangzhou University (17 documents), Rutgers University (13 documents), Concordia University (10 documents), Northeastern University (9 documents), and the University of Utah (9 documents) are identified as the top leading five institutions regarding the published research pertinent to the CA_GPR domain. Table 2 reports the most influential authors working on CA_NDT research according to h-index, g-index, and m-index. It is worth mentioning that the authors mentioned herein are the ones who accomplished an h-index of more than three. With regards to h-index, the top-ranked authors are Dinh K (10), Gucunski N (9), Zayed T (8), Liu H (6), and Yazdani N (5). In terms of g-index, Dinh K (11), Gucunski N (11), Zayed T (10), Liu H (6), and Yazdani N (5) are the forerunners. Furthermore, the gauged m-index demonstrates Dinh K (1.11), Liu H (1), Feng J (1), Hoxha E (1), Xiao J (1), and Yang L (1) are the top influential scholars.

Table 2: Production of leading authors in the research on CCS_NDT

Author	**h-index**	**g-index**	**m-index**
DINH K	10	11	1.11
GUCUNSKI N	9	11	0.82
ZAYED T	8	10	0.89
LIU H	6	6	1
YAZDANI N	5	5	0.5
BALAYSSAC J-P	4	4	0.18
CUI J	4	4	0.67
DUONG TH	4	4	0.5
HASAN MI	4	4	0.4
HELMERICH R	4	4	0.4
HONG S	4	4	0.4
WIGGENHAUSER H	4	4	0.31

3.3 Keywords Analysis

This section expounds on the most frequent keywords, keyword co-occurrence map, and its temporal evolution.

3.3.1 Most occurred author keywords

The eighteen most frequently occurring author keywords are shown in Table 3. As presented in Table 3, at the top of the list are ground penetrating radar, non-destructive testing, and their synonyms. Authors usually use them to tag their publications in this domain. Other keywords frequently used by the authors to index their publications include bridge decks, concrete, reinforcing bars, and condition evaluation. These keywords resemble the general description of the research direction.

The keywords of steel bars corrosion, rebar recognition, and rebar diameter represent the main applications of GPR in the inspection and assessment of concrete structures. The techniques used to perform condition assessment using GPR are characterized by a combination of keywords, including deep learning, hyperbolas, image processing, and convolutional neural networks. The presence of automation in the list of most frequently occurring keywords indicates a clear trend in asset condition assessment, including using GPR to inspect concrete structures.

Table 3: Most occurred author keywords.

Keyword	**Occurrence**	**Total Link Strength**
Ground penetrating radar	95	430
Non-destructive testing	34	172
Steel bars corrosion	19	96
Concrete	18	87
Bridge decks	14	72
Reinforcing bars	11	45
Deterioration	9	51
Rebar recognition	9	39
Condition assessment	8	42
Deep learning	8	43
Rebar diameter	8	37
Bridge inspection	7	31
Reinforced concrete	7	36
Concrete cover	6	25
Hyperbolas	6	32

Automation	5	32
Convolutional neural network	5	32
Image processing	5	24

3.3.2 Keyword co-occurrence map

Keywords of the studied articles were analyzed using VOSviewer to derive the co-occurrence map and identify the major research directions using keywords' clustering. Fig. 4 shows the co-occurrence map of the analyzed keywords. The size of the nodes corresponds to the occurrence of the keywords, whereas the link thickness shows the connection strength between keywords. The different clusters were made visually distinguishable by color variation. Table 4 summarizes the attributes and the description of the resultant clusters.

As presented in Table 4, the first cluster, highlighted in red, constitutes the general usage of GPR as a non-destructive technique for inspecting concrete structures. It includes the classical use of GPR for concrete inspection. The second cluster of keywords, highlighted in purple, indicates methods for automated rebar recognition from GPR images. The methods mainly include machine learning, deep learning, and image processing. In addition, automation and robotics indicate the emerging research trend associated with the use of GPR for bridge deck inspection. The third cluster of keywords, highlighted in green, indicates several major applications of GPR in concrete structures that constitute locating rebars, identifying their diameter, and evaluating their corrosiveness. The methods used include numerical analysis that also correlated with the appearance of other keywords, including time domain analysis, finite difference time domain method, and wave propagation. The last cluster, highlighted in yellow, constitutes keywords that represent a category of studies investigating the effect of different factors on the GPR signals, such as moisture and chloride contamination.

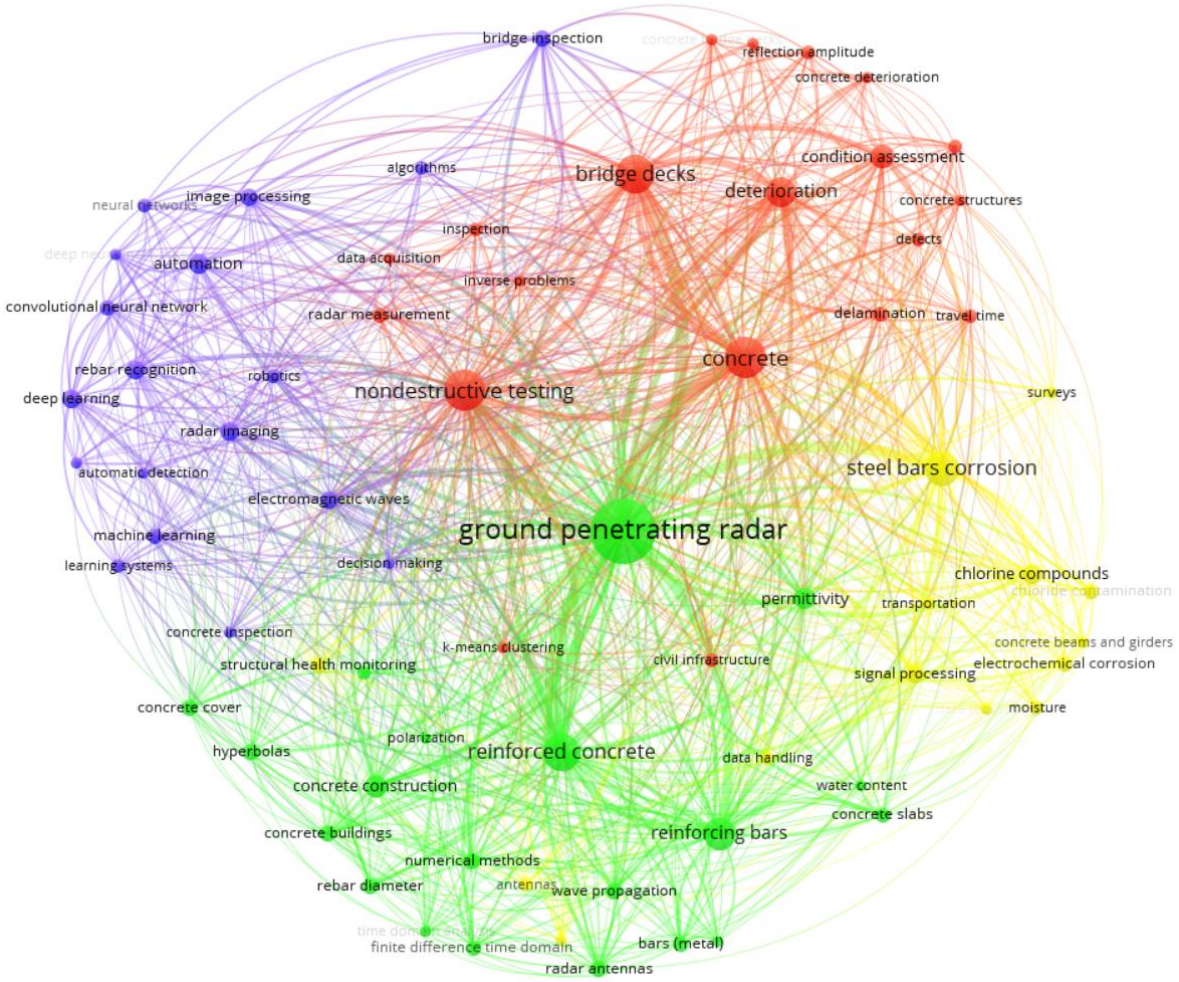

Fig. 4: Keywords mapping shows the keyword clustering.

Table 4: Keyword cluster description.

Cluster No.	Keywords No.	Color	Cluster description
1	20	Red	The general applications of GPR for inspecting concrete structure deterioration inspection.
2	18	Purple	The emerging research trend in the automation of GPR analysis and rebar recognition based on Bscan-Images using techniques such as computer vision, machine learning, automation, and robotics.
3	20	Green	The main applications of GPR in concrete structures that are associated with reinforced corrosion.
4	14	Yellow	The study of the impact affecting factors on the GPR signal attenuation & the experimental work related to them.

3.3.3 Temporal analysis:

Fig. 5 presents the results of the temporal analysis of the most occurred keywords conducted using VOSviewer. The mapping of the keywords represents their co-occurrence. The node size

196 indicates the occurrence of the keywords, whereas the link thickness indicates the linkage
197 strength of the connected keywords. The color of the nodes indicates their average publication
198 year. The temporal analysis is utilized to conclude multiple interesting remarks. Fig. 5 vividly
199 reinstates the fact that most of the articles were published in the last few years. The generally
200 used keywords of ground penetrating radar, concrete, bridge decks, and non-destructive
201 techniques are associated with the period extending between 2014 and 2018.

202 Seven keywords (10%) were found to be predominantly used before 2014, including algorithms
203 and neural networks. The use of these keywords declined after 2014, such that the average year
204 of publication was below 2014. Twenty-five keywords (35%) have an average year of
205 publication of at least 2018. These keywords indicate a research trend in automating the
206 inspection of bridge decks using GPR. These keywords include automation and robotics. Also,
207 it includes machine learning, learning systems, deep learning, neural networks, and
208 convolutional neural networks.

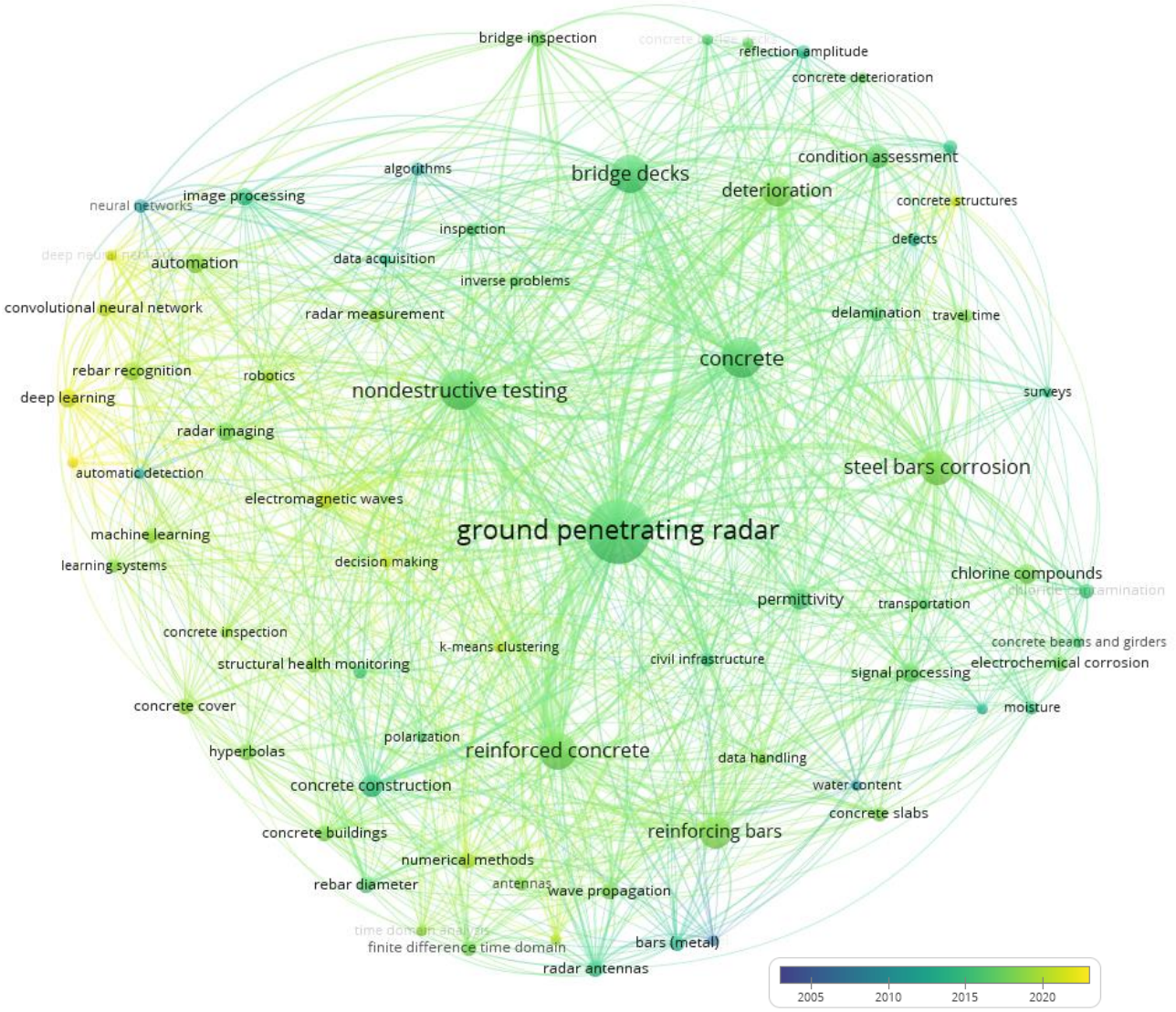

Fig. 5: Keyword mapping shows the overlay visualization over time.

4 SYSTEMATIC REVIEW ANALYSIS

Although scientometric analysis has its advantages, it is insufficient to fully comprehend the topic being studied. Therefore, a comprehensive systematic review was conducted to gain a deeper comprehension of the employment of GPR in corrosion assessment. As shown in Fig. 6, the reviewed articles were discovered to originate from either laboratory trials, field studies, or a blend of both. The field studies, which mainly encompass bridge dicks, concrete slabs, and tunnels, primarily focus on developing reliable GPR interpretation techniques. Conversely, the

articles that originated from laboratory primarily aimed to comprehend the factors that impact electromagnetic waves in concrete materials.

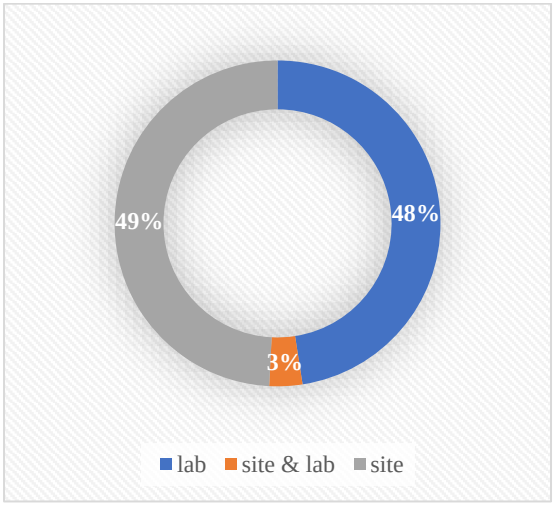

Fig. 6: Laboratory and site GPR inspection.

4.1 GPR performance analysis for corrosion assessment

Evaluating the performance of NDTs techniques in terms of time, cost, and reliability is crucial for selecting the most suitable technique for the intended application. In this regard, Abdelkhalek et al. [21] delivered a comparative analysis for performance assessment of nine NDTs, namely GPR, Half-Cell Potential (HCP), Polarization Resistance (PR), Electrical Resistance (ER), Impact-Echo (IE), Ultrasonic Pulse Echo (UPE), Ultrasonic Surface Wave (USW), Infrared Thermography (IRT), and Digital Camera. The comparison addressed some criteria like defect detection, ease of implementation, cost, speed, and performance under different circumstances. It was elucidated that GPR was the top-ranked corrosion assessment NDT, followed by HCP, ER, and PR respectively.

Limited research studies delved into the performance of GPR in corrosion assessment in terms of speed and cost. Table 5 depicts the estimated inspection and analysis speeds of GPR. For instance, Abdelkhalek and Zayed [22] identified GPR as the third fastest NDT behind digital photogrammetry and IRT. Their analysis was predicated on experts' judgments using multi-

criteria decision analysis. In another study, Taylor et al. [23] indicated that the estimated data collection and analysis speeds of a ground-coupled antenna mounted on a hand-dragged cart were 4,800 ft^2/hr and 3,200 ft^2/hr, respectively. As for the air-coupled GPR mounted on a vehicle, the estimated data collection and analysis speeds were 12,000 ft^2/hr and 3,200 ft^2/hr, respectively. In their study, Taylor et al.[23] identified GPR as the second-fastest NDT behind IRT. Similarly, Gucunski et al.[24] conducted an inspection survey for a concrete deck using a ground-coupled GPR and grid spacing of 2 ft × 2 ft. Likewise, GPR was ranked as the second fastest NDT after IR, with data collection and analysis speeds of 2,188 ft2/hr and 252 ft2/hr, respectively. Notably, the reported data collection speed can be shortened by increasing the number of participants [24]. In addition, the analysis speed was assumed based on the conventional analysis methods, in which the majority of the time is consumed during the visual interpretation or the manual rebar picking. Thus, the time could be shortened using automated analysis methods.

Regarding the cost dimension, Gucunski et al. [24] deduced that the inspection costs with and without traffic control were equal to \$0.78/ft^2 and \$0.6/ft^2, respectively. Despite the above-mentioned efforts, Abdelkhalek [25] disclosed that there are still other factors that impact the speed and cost of the bridge inspection process. The factors encompassing grid line spacing, preparation time, deck area, and condition rating are commonly overlooked and need to be considered in the time and cost simulation. In this context, Abdelkhalek [25] designed an optimization model that aimed to simultaneously maximize the performance of the GPR inspection system by minimizing the inspection time and inspection cost. In the developed model, a traffic control strategy was incorporated so that the overall costs and respective traffic delays could be modeled and diminished.

Table 5: Data collection and analysis speeds for GPR

	Gucunski et al.[24]	**Taylor et al.**[23]

Non-destructive technique	Data collection speed (ft^2/hr)	Data analysis speed (ft^2/hr)	Data collection speed (ft^2/hr)	Data analysis speed (ft^2/hr)
Ground-coupled GPR	2,313[a]	800[a]	4,800	3,200
	2,871[b]	600[b]		
	2,188[c]	252[c]		
Air-coupled GPR	N/A	N/A	12,000	3,200

The symbols "a," "b," and "c" denote 9, 8, and 5 participants were involved in the data collection and analysis processes.

In addition to time and cost analysis, several studies compared the deterioration maps generated by GPR with the maps generated by other NDTs. These comparisons aimed to assess the level of agreement and disagreement between the maps using spatial correlation analysis as the quantification metric. For instance, Gucunski et al. [26] conducted a repeatability analysis to optimize GPR thresholds that provide a consistent corrosion localization. The condition mapping was compared with other NDTs and exhibited 71.4% agreement between ER and GPR and 75.1% agreement between HCP and GPR. In a similar study, Barnes et al. [17] predicted CD and HCP deterioration maps using optimized GPR thresholds. The results exhibited negligibly small errors between the expected and actual results. The authors pointed out that the tested bridge deck was not highly deteriorated and emphasized the necessity for testing the established relationship on more severely deteriorated decks. In another study, after testing severely deteriorated decks, Maser et al. [15] pointed out that a strong spatial correlation (90.2%) was exhibited between GPR and HCP, and it was relatively higher than the correlation (79.3%) between GPR and IE, which means that GPR is more effective in corrosion assessment compared to its performance in detecting delamination. This complies with the analysis of Robison et al. [27], who exemplified that a high correlation (82%) was maintained between ground-coupled GPR and CD in relatively healthy concrete decks. Yet, the degree of correlation fell dramatically to 34% in extensively damaged bridge decks. The same applies to IE, where the correlation with ground-coupled GPR dropped remarkably from 79% to 51% in

the more deteriorated bridge. These outcomes indicate that GPR is more applicable for early corrosion assessment than for delaminated detection.

The preceding investigations proved a robust correlation between electrical (ER), electrochemical (HCP), and electromagnetic (GPR) methods. Nevertheless, the strength of this correlation depends on the selected GPR thresholds and the method employed for GPR scan analysis [17]. On the other hand, when compared with IE and CD, GPR exhibited limited effectiveness in detecting delamination, which makes the GPR more suitable for early-stage corrosion assessment. Hence, GPR enables deterioration prediction and facilitates the implementation of predictive maintenance during the early stages of the structures' lifespan [15].

4.2 Influential Factors on GPR Signal

The reviewed literature reveals widespread confusion concerning the causes of GPR signal attenuation and its relation with the corrosiveness of the concrete environment. As shown in Fig. 7, a combination of technical, physical, and environmental factors is often blamed for amplitude variations. However, the effect of these phenomena on signal attenuation is intricate and has contradictory arguments.

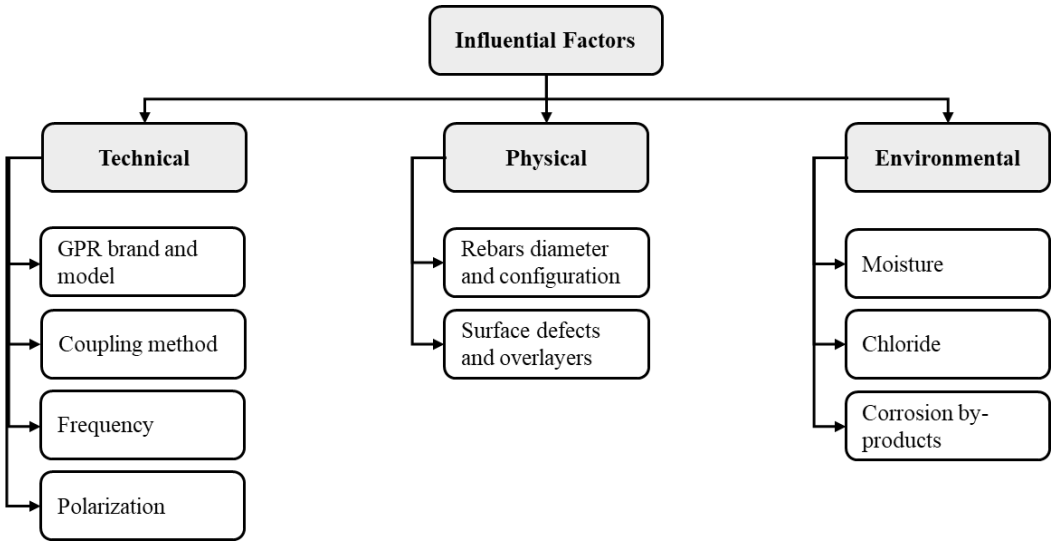

Fig. 7: Influential factors on GPR signal.

4.2.1 Technical factors

Numerous authors have illustrated the technical and theoretical principles of GPR [28–30]. GPR mainly transmits electromagnetic (EM) waves that propagate through different materials and records the reflections' power in parallel with the two-way travel time. A typical GPR inspection requires a ground-coupled or horn (air-launched) antenna to scan the structure under inspection. The propagation of GPR pulses in concrete structures is mainly influenced by the EM property of the concrete medium. The EM property is a combination of the dielectric permittivity (Ɛ), the electrical conductivity (σ), and the magnetic permeability (μ) [29]. Since concrete is a nonmagnetic material, the concrete's magnetic permeability (μ) is assumed to be equal to the free space permeability (μ_0) [31]. Thus, dielectric relaxation caused by (Ɛ) and electrical conduction caused by (σ) predominantly control the EM wave attenuation. The EM wave attenuation manifests as a decrease in the wave's amplitude and a downshift of the central frequency. As given in Eq. (2), the attenuation of electromagnetic (EM) waves (α) is a function of electrical conductivity (σ), dielectric permittivity (Ɛ), and wave's angular frequency (ω) [32].

$$\alpha = \omega \sqrt{\frac{\mu_0 \varepsilon}{2}} . \sqrt{\left(\sqrt{1 + \left(\frac{\sigma}{\omega \varepsilon}\right)^2} - 1\right)} \qquad (2)$$

In the frequency range of (100 – 3000MHz), EM wave behavior in concrete is dominated by Ɛ and σ, and it is challenging to distinguish their separated effects [33]. Thus, these two properties have been integrated into the effective permittivity ε_e. The effective permittivity is defined by Eq. (3), where ε_e is a complex combination of ε_e' and ε_e'' . ε_e' refers to the dielectric media's ability to store EM energy and influence EM wave velocity. The imaginary part ε_e'' refers to

the loss factor that represents the energy transferred in conduction or lost by energy dissipation due to dielectric relaxation (absorption)[34].

$$\varepsilon_e = \varepsilon + \left(\frac{\sigma}{i\omega}\right) = (\varepsilon' - i\varepsilon'') + \left(\frac{\sigma' + i\sigma''}{i\omega}\right) = \varepsilon'_e - i\varepsilon''_e \quad (3)$$

Effective permittivity is a complex attribute expressing a material's capacity to be polarized in an external electric field. In practice, the material's effective permittivity is related to the permittivity of free space ε_0 to generate the relative permittivity ε_r. As defined in Eq. (4), the real part of the relative permittivity (ε'_r) is usually known as the dielectric constant, and it mainly controls the propagation velocity (*v)*, as shown in Eq. (5). The imaginary part of the relative permittivity (ε''_r) is known as the loss factor and mainly represents the EM energy losses [34].

$$\varepsilon_r = \frac{\varepsilon_e}{\varepsilon_0} = \varepsilon'_r - i.\,\varepsilon''_r \quad (4)$$

$$\varepsilon'_r = \left(\frac{c}{v}\right)^2 \quad (5)$$

c refers to the propagation velocity of electromagnetic waves in free space (3×10^8 m/s).

As shown in Fig. 8, the received EM wave comprises multiple reflections. In air-coupled GPR, the first portion of the received wave is usually caused by the direct energy traveled from the transmitting to the receiving antenna (AW). The second reflected peak represents the reflected energy along the air–material interface (GW). However, for ground-coupled antennas, the GW and the AW merge to appear as a direct wave (DW) due to their small time difference [35]. The other portions of the reflected wave (RW) represent the reflected energy from other interfaces, including rebars. Eq. (6) illustrates the reflection coefficient (ρ) at the interface of

two mediums, which expresses the relationship between the transmitted and reflected energy as a function of the relative permittivities' of upper and lower materials [36,37].

$$\rho = \frac{\sqrt{\varepsilon_{r1}} - \sqrt{\varepsilon_{r2}}}{\sqrt{\varepsilon_{r1}} + \sqrt{\varepsilon_{r2}}} \quad (6)$$

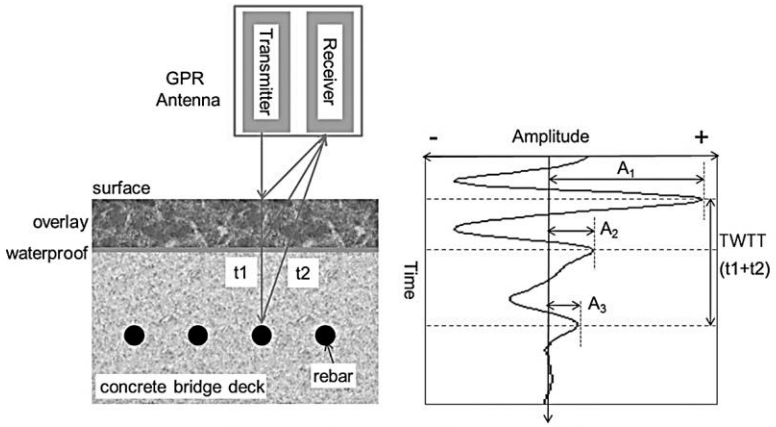

Fig. 8: GPR basic principle [10].

GPR brand and model:

As outlined in Fig. 9, the GPR system primarily comprises a control unit connected to an antenna, allowing data collection in time mode or distance mode when accompanied by a distance measurement encoder (DMI). Subsequently, the acquired data is typically subjected to analysis using specialized software. The capability of the GPR systems and processing software may affect the interpretation results. However, no investigation has undertaken a comparison in this aspect. In this review, the available GPR systems were analyzed to identify prominent manufacturers in the GPR industry in the context of the current study.

(a) (b) (c)

Fig. 9: GPR system components, where (a) is the GPR antenna, (b) is the control unit, and (c) is the DMI.

Table 6 presents the details of the identified manufacturers, examples of their GPR systems, and software packages. Ten manufacturers based in seven countries were identified. It was observed that manufacturers produce different GPR systems customized for various applications, including concrete and bridge inspections. Customized software packages are also available for data collection and analysis. For example, Geophysical Survey System Inc (GSSI) has introduced multiple GPR systems and software packages tailored for specific purposes. GSSI GPR systems include the StructureScan Pro and ProBridgeScan, which incorporate the SIR 4000 controller unit and antennas of different frequencies (1.6 and 2.6 GHz) [38]. However, many researchers customized their systems by using a different combination of GSSI controlling units (SIR 2000, SIR 3000, and SIR 4000) and antennas of different frequencies (e.g., 1.5, 1.6, 2, 2.6 GHz). GSSI also provides software packages for data collection and processing under the name of RADAN. Another prominent company is Ingegneria dei Sistemi (IDS). Researchers used different IDS GPR systems, such as C-thrue, RIS MF Hi-Mod, and RIS Hi-BrigHT. Additionally, the company provided data collection and processing software, such as K2 FastWave, GRED HD Basic, and GRED HD 3D. It is worth noting that multiple studies reported the use of the gprMAX software for conducting simulation analysis.

371 Table 6: GPR systems manufacturers.

Reference	Manufacturer	Origin	GPR systems	Software packages
[38]	Geophysical Survey System Inc. (GSSI)	USA	StructureScan Pro ProBridgeScan	RADAN
[39]	Ingegneria dei Sistemi (IDS)	Italy	C-thrue RIS MF Hi-Mod RIS Hi-BrigHT	K2 FastWave GRED HD Basic GRED HD 3D
[40]	Japan Radio Co., Ltd. (JRC)	Japan	NJJ-105	Radar 3D_Light RC report maker
[41]	Sensors & Software Inc. (SSI)	Canada	PulseEKKO Pro NOGGIN CONQUEST 100	EKKO_Project™ GPR Software
[42]	Screening Eagle Technologies (SET) (Proceq).	Switzerland	GP8000 GS8100 GS8800	Proceq GPR App
[43]	Guideline Geo.* (GG MALA)	Sweden	MALÅ MIRA HDR MALÅ Ground Explorer	MALÅ Vision
[44]	Utsi Electronics Ltd. (Utsi)	UK	Groundvue 3	Wall Analyser
[45]	Penetradar Corporation (Penetradar)	USA	IRIS GPR	IRIS Software
[46]	Radar Systems, Inc. (RSI)	Latvia	Zond-12e	Prism2 software
[47]	ImpulseRadar	Sweden	Impulse PLT 600	ViewPoint App Condor

372 * Previously known as MALA GeoScience.

373 Data processing is important to ensure an accurate interpretation of GPR data. The software
374 packages summarized in Table 6 are not open-source and are exclusively designed to be
375 compatible with their respective developers' GPR systems. Table 7 depicts the other alternative
376 software packages and illustrates their corresponding features. For instance, GPRPy is an open-
377 source processing software compatible with various GPR systems. It offers a user-friendly
378 graphical interface and is built on Python, making it compatible with various operating systems
379 [48]. Similarly, Reflexw [49] and GPRSoft [50], which are not open-source, offer capable

processing and simulation features and are compatible with most GPR systems. However, these software require licenses. In addition, Geolitix provides advanced analysis and interpretation tool that enables cloud computing for efficient and fast analysis [51]. Moreover, GPRmax is a renowned GPR simulation tool known for its detailed numerical simulation of GPR with high spatial resolution [52]. Additionally, multiple studies indicated the further processing of data using MATLAB codes to overcome the limitations of commercial software [58–60].

Table 7: GPR processing software.

Reference	**GPR processing software**	**License**	**Features**
[48]	GPRPy	Open source	Compatible with a range of GPR systems, it includes a graphical interface that makes learning easy.
[52]	GPRmax	Open source	Allows for detailed numerical simulation of GPR with high spatial resolution.
[49]	Reflexw	License required.	GPR and seismic analysis software that enables 2D and 3D processing and allows modeling and simulation.
[50]	GPRSoft	License required.	Compatible with a range of GPR systems, it enables high-quality preprocessing and interpretation.
[51]	Geolitix	Open source	Offers a cloud computing platform. Compatible with a range of GPR systems and enables 2D and 3D processing.

The popularity of GPR systems among researchers is summarized in Fig. 10. As depicted in Fig. 10, GSSI stands out as the most widely used system, with 47 articles reporting its utilization. The second, third, and fourth most favored GPR manufacturers by the researchers in the context of the current study are IDS, JRC, and GG MALA, respectively. Other less popular GPR system manufacturers in the context of the revised articles include SSI, SET, Utsi, Pentradar, RSI, and ImpulseRadar. It's important to note that certain studies either reported the manufacturing of their own GPR systems [53] or the utilization of their own developed processing software [14,54,55]. However, there exists a scarcity of research highlighting the influence of various brands on the collected data. Moreover, the literature lacks a comprehensive comparison of the capabilities of commercial software.

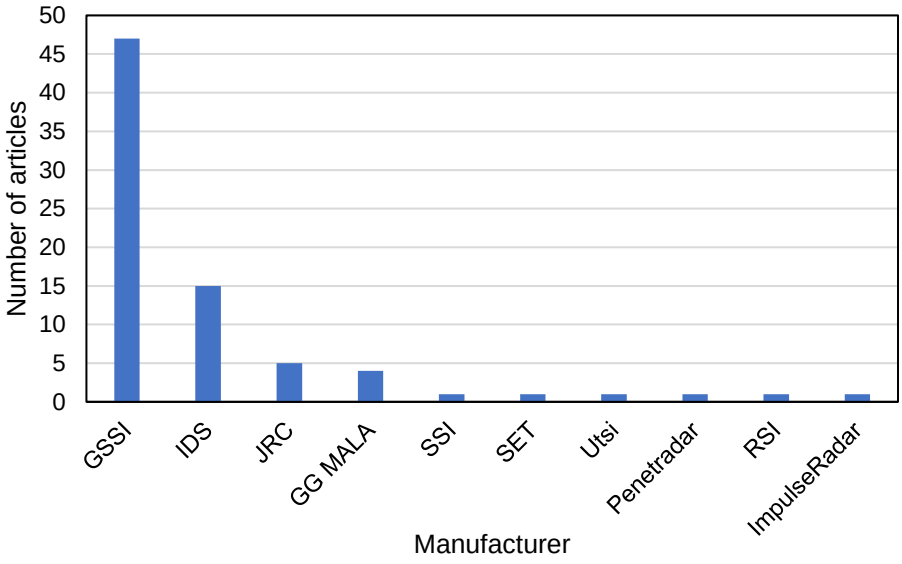

Fig. 10: Popularity of GPR systems manufacturers.

GPR coupling method:

Based on the operation methods, there are two types of GPR systems: air-coupled and ground-coupled. In the air-coupled system, the antenna is usually attached to a moving vehicle with an offset in the range of 15–50 cm from the ground. This ensures a high-speed survey with minimum traffic interruption. However, this offset reduces the scanned image quality. In reinforcement corrosion assessment, the air-coupled GPR is mainly used for large-scale surveys that include multiple concrete bridges [10,56]. In addition, it could be complementary to ground-coupled devices to trace the reinforcement distribution and plan the survey tracks [57]. On the contrary, the ground-coupled system is usually attached to a pushing cart that is manually dragged as it requires direct contact with the surface. This system provides better-scanned image quality and is more common for detailed reinforcement inspection [15]. Indeed, the frequency of used coupling systems shown in Fig. 11 shows that the majority (82%) of corrosion assessment research uses the ground coupled system.

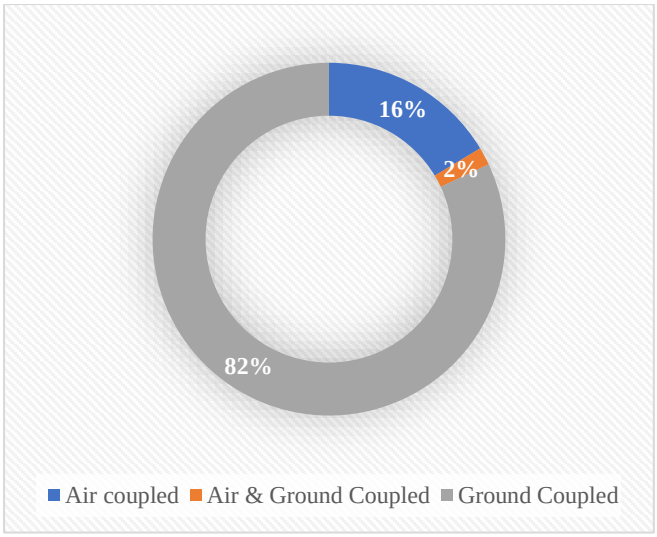

Fig. 11: Distribution of GPR Coupling systems.

GPR antenna frequency:

According to Eq. (2), the attenuation of EM wave amplitude directly correlates to wave frequency. The frequency-dependent attenuation mechanism states that the higher the frequency, the greater the attenuation rate and the higher the level of details [58]. In practice, GPR antennas operate over frequencies ranging from 10 MHz to 2.6 GHz, and the researchers utilize GPR frequencies that suit their objectives [59]. According to the revised literature, Fig. 12 shows the most commonly used frequencies for reinforcement inspection. From the review, it can be concluded that the majority of research (40%) uses 1.5 GHz and 1.6 GHz frequencies as they achieve an optimum level of detail and penetration depth for bridge deck assessment. On the same note, higher frequencies in the range of (2-2.6) GHz account for 32% of the used GPR frequencies. These high frequencies allow for a higher level of detail. However, they are not preferable for structures with deep covers or overlays and have mainly been used for small-scale surveys inside the laboratories. Lower frequencies of (0.9-1) that account for 21% of the used frequencies have been mainly used with air-coupled GPR devices.

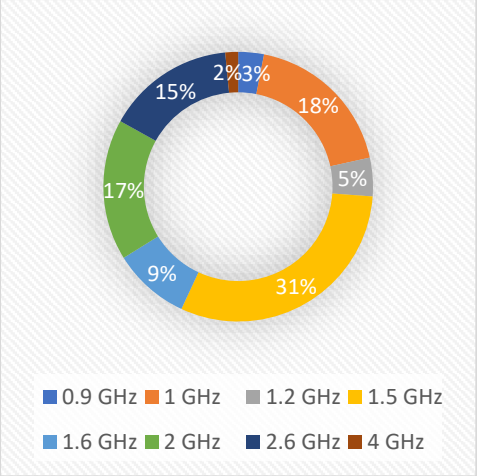

Fig. 12: Distribution of GPR frequencies

GPR polarization and number of receiving antennas:

At a minimum, GPR devices have two antennas, one transmitting and one receiving antenna. Most GPR devices use dipole antennas, which are the simplest and most commonly used antenna. Dipole antennas use a center-fed driven element for transmitting or receiving electromagnetic wave energy [60]. Thus, the produced electromagnetic wave is a linearly polarized (oriented) wave whose direction is perpendicular to the long axis of the antenna, as shown in Fig. 13 (a). Polarization, which is a representation of the scan direction and antenna orientation, plays a fundamental role in the selection of measuring strategy. Cross-Polarization (H-polarization) and Co-Polarization (E-polarization) are the most commonly used polarization methods [61]. In Co-Polarization, the dipoles are oriented parallel to the direction of the reinforcement layout. Conversely, in Cross-Polarization, the dipoles are oriented perpendicular to the direction of the reinforcement layout, as shown in Fig. 13 (b).

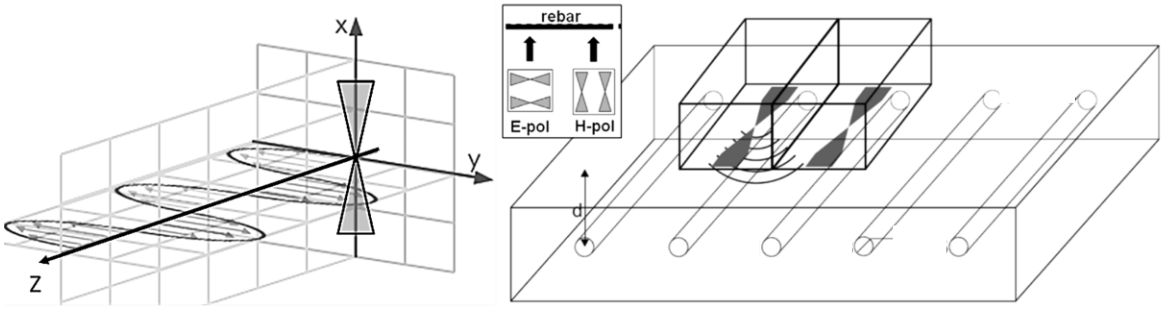

(a) (b)

Fig. 13: (a) The Dipole antennas EM wave. (b) GPR Cross-Polarization (H-polarization) and Co-Polarization (E-polarization).

The received EM wave is a function of the antenna's polarization and rebar scattering properties [60]. Therefore, GPR polarization is critical to achieving the best scanning results considering the orientation, shape, size, and dialectical properties of the buried objects. For instance, Co-Polarization produces the best accuracy for shallow reinforcement imaging, while CrossPolarization is considered better for recognizing deep targets [62,63]. As illustrated in Fig. 14, 97% of the literature utilized Co-Polarization for reinforcement assessment. Additionally, a limited number of scholars have integrated Cross-Polarization and Co-Polarization antennas to develop novel methods for reinforcement assessment. For instance, Hugenschmidt et al. [64] and Dinh et al. [62] Have utilized dual polarization to generate high-resolution 3D images (C-Scans) for reinforced concrete structures. In addition, multiple researchers [32,61,65] have used the ratio between Co-Polarization and Cross-Polarization results to estimate the reinforcement radius. On the same note, Liu et al. [53] have used dual polarization to study the scattering mechanism of rebars and detect early-stage rebar corrosion. Other researchers [66,67] have used GPR devices with dual-receiving antennas, with both antennas at the CoPolarization position, to estimate rebar depth and EM wave propagation velocity.

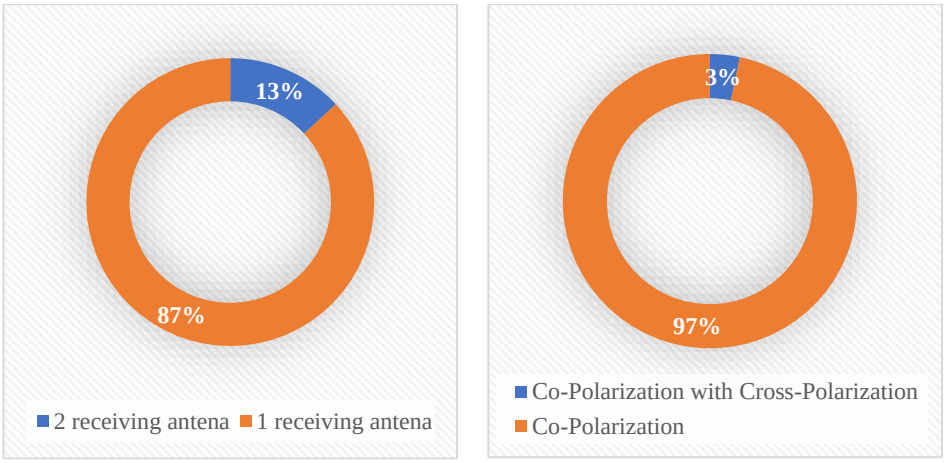

(a) (b)

Fig. 14: Types of GPR based on (a) the number of receiving antennas and (b) polarization method.

4.2.2 Physical-related factors

There are a variety of physical factors that could affect the interpretation results of GPR. According to the available literature, these factors can be mainly related to steel rebars, concrete medium, surface anomalies, and overlays.

Rebars diameter and configuration effect on GPR signals:

As summarized in Table 8, rebar diameter, orientation, spacing, and cover depth can impact the reflected wave amplitudes and B-scans' sharpness. In this regard, Hasan and Yazdani [68] and Zhou et al. [69] studied the effect of rebar diameters' on the normalized amplitude; the results indicate a linear relationship between the diameter reduction and the normalized amplitude values. In similar studies, Sahamitmongkol [70] and Leucci [32] have used a 1 GHz GPR antenna to experimentally study the effect of rebar diameter and orientation on the reflected amplitude. The results also show that RW amplitude increases with rebar diameter, and the amplitude is maximized when the scanning angle is perpendicular to the rebar's layout. On the same note, multiple researchers [68,71,72] illustrated that rebar diameter reduction due to corrosion reduces the reflected amplitude and B-scans' sharpness.

The rebar distribution can also affect the GPR scan result. For instance, reinforcement splicing alters the B-scan's hyperbolic shapes and increases the amplitude value, and transverse reinforcement can reduce the reflected amplitude and appear in the B-scan image as a line over hyperbolas [73]. However, compared to the previously mentioned factors, the literature emphasizes that cover depth has the most effect on EM wave attenuation [17,74–76].

Table 8: Rebars diameter and configuration effect on GPR signals

Reference	Freq	Method	Property	Amplitude
[70]	1 GHz	Lab-experiment.	Diameter ↑	↑
			Scanning angle	Max at 90 °
[32]	1 GHz	Lab-experiment	Diameters ↑	↑
[74]	2.6 GHz	Lab- experiment and numerical simulation.	Diameter ↑	↑
			Cover depth ↑	↓
[68]	2.6 GHz	Lab-experiment.	Diameters ↑	↑
[71] [69] [72]	1.6 GHz	Lab-experiment.	Diameters ↑	↑
[17] [76][75]	1.5 GHz	Bridge deck assessment	Cover depth ↑	↓

Surface defects and overlayers' effects on GPR signals:

As summarized in Table 9, surface distresses and anomalies alter the reflection coefficients and EM wave attenuation [77]. Surface properties such as smoothness constrain EM energy penetration into the concrete deck [75]. Tarussov et al. [14] studied the effect of different surface anomalies on the reflected amplitude; the results indicate that most surface cracks are not large enough to affect the radar signal, and only large cracks of 2 mm or broader can cause attenuation to the GPR signal. Similarly, Hong et al. [78] and Tesic et al. [79] found that cracks up to 1 mm cause a negligible impact on the GPR amplitude. However, the presence of cracks can increase the moisture and chloride ingress to the concrete cover and exuberate the signal attenuation [76].

Overlays increase the durability of concrete decks and extend the lifespan of deteriorated concrete decks. However, overlays pose challenges to corrosion evaluation in concrete decks. In this regard, Meng et al. [80] conducted laboratory experiments to experience the effect of seven types of overlays on GPR signals. Accordingly, Meng et al. [80] found that materials of

polyester polymer overlay, asphalt overlay with a liquid membrane, and silica fume-modified concrete overlay can influence GPR measurements and result in misleading corrosion results. On the other hand, the materials of epoxy polymer concrete overlay, asphalt overlay with a sheet membrane, latex-modified concrete overlay, and asphalt overlay without a membrane have a limited effect on GPR measurement and allow for accurate corrosion detection. However, the debonding of any coating layer may alter the GPR reflected signal depending on the water presence at the interface [77].

Table 9: Surface defects and overlayers' effects on GPR signals.

Reference	Freq	Experiment	Method	Result
[14]	2 GHz	Bridge deck	Numerical and visual interpretation.	Cracks up to 2 mm have a limited effect on the amplitude.
[80]	1.5 GHz	Laboratory experiment of 7 types of overlays	Numerical interpretation.	Some types of overlays reduce the GPR accuracy.
[79]	2.7 GHz	Laboratory accelerated corrosion	Numerical interpretation.	Cracks up to 1 mm do not affect GPR accuracy.
[78]	2 GHz	Numerical simulation for cracks.	Numerical interpretation.	The filling of concrete cracks with corrosion by-products increases the reflected amplitude.

4.2.3 Environmental-related factors

This sub-section delves into the literature that examined the effects of corrosion, chloride contamination, moisture, and other environmental variables on EM waves.

Moisture content effect on GPR signals:

As discussed in section 4.2.1, effective concrete permittivity is a complex combination of materials' conductivity and permittivity. As shown in Fig. 15, conductivity and permittivity are dependent on frequency and moisture content [81]. Accordingly, the relative permittivity at a specific frequency varies according to the moisture content of the concrete medium. Consequently, moisture affects the EM wave propagation speed and amplitude attenuation.

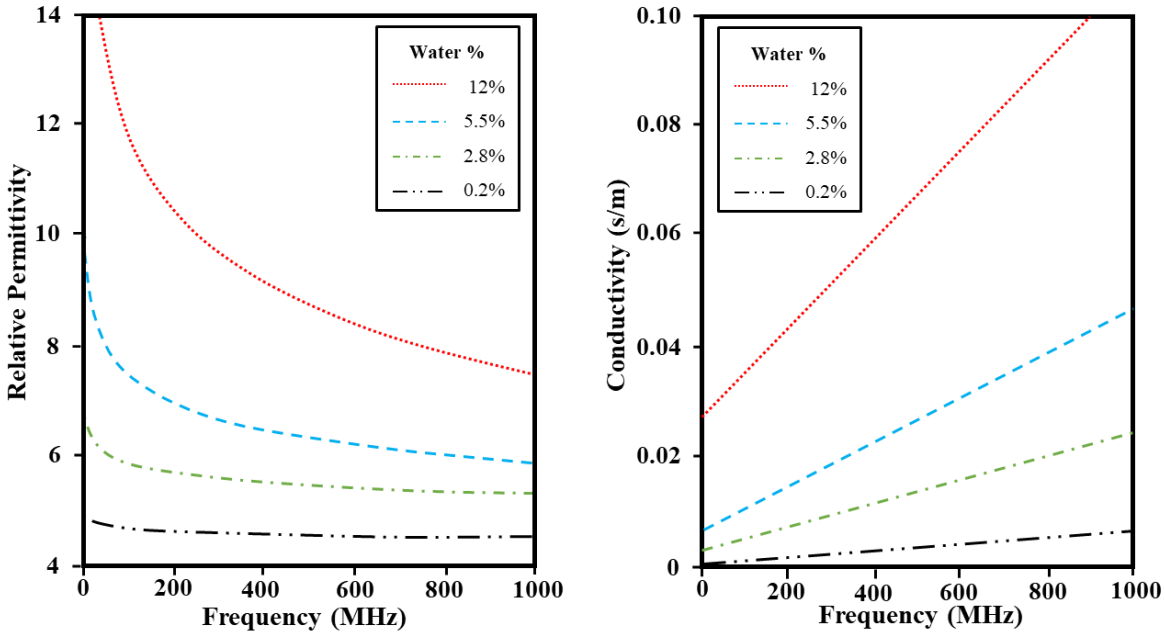

Fig. 15: Permittivity and conductivity variation with frequency and moisture content [81].

Multiple researchers have conducted experimental investigations attempting to understand the relationship between moisture content, RW amplitude attenuation rate, DW amplitude attenuation, dielectric constant, and EM wave propagation velocity [14,29,34,82–86]. The results clearly show that moisture content increases the attenuation rate and slows down the EM wave, so the slap thickness appears greater than it is.

Table 10 provides a summary of experiments that investigated the relationship between moisture content and the corresponding dielectric constant and wave velocity. The data derived from these studies were used to gain a better understanding of these relationships. Table 11 summarizes the statistical analysis of the relationships. Accordingly, the linear relationships developed by the different studies are statistically significant, with p-values less than 0.05 and R^2 values exceeding 95% for all regression models. Similarly, the regression model developed using all data was found to be significant, with p-values much lower than 0.05 and R^2 values larger than 0.89. Thus, it can be concluded that the null hypothesis can be rejected, and the established relationships are statistically significant.

Fig. 16 and Fig. 17 present the linear regressions for the combined data extracted from all

studies. Also, box plots were employed to compare the results of regressions developed by different studies with those developed using the combined dataset. Accordingly, Fig. 16 presents the representative linear relationship between moisture content and dielectric constant, and Fig. 17 presents the representative relationship between moisture content and wave propagation velocity. The box plots show that the regression models developed by the four studies exhibit higher consistency for moisture content within the range of 2% to 6%. However, the deviations between the four studies gradually increase when moisture content surpasses 6%.

Depending on the discussed relation between wave velocity and moisture content, Agred et al. [67] have developed an algorithm using a GPR device with two receiving antennas to measure the rebars' depth and wave velocity inside the concrete cover simultaneously with a 90% accuracy. Subsequently, wave velocity was used to map the moisture content in the concrete cover. Moisture content can infer the porosity of the concrete cover and can be used to indicate concrete soundness[87].

Table 10: Moisture content effect on permittivity and wave velocity.

Reference	**Frequency GH**	**Moisture content %**	**Relative permittivity**	**Wave velocity (cm/ns)**
[83]	1.5 GHz	[0, 5, 10, 12.5, 15]	[4.4, 7.5, 11.5, 13, 14.8]	[14.3, 11.0, 8.8, 8.3, 7.8]
[84]	1.5 GHz	[0, 2.5, 5, 9.5, 14]	[5.5, 6.5, 8, 10.3, 12]	[12.8, 11.8, 10.6, 9.3, 8.7]
[85]	1.5 GHz	[0, 2.5, 5, 7.5, 10.1]	[4.3, 6.5, 8.4, 10, 11.4]	[14.5, 11.8, 10.4, 9.5, 8.9]
[86]	2 GHz	[0, 2.5, 5, 7.5, 10]	[4.5, 6, 8.5, 10, 12]	[14.1, 12.2, 10.3, 9.5, 8.7]

Table 11: Summary of the statistical analysis of the relationship between moisture content effect on permittivity and wave velocity.

Reference	**Moisture content % vs. Relative permittivity**			**Moisture content % vs. Wave velocity (cm/ns)**		
	Equation	**R^2**	**P-value**	**Equation**	**R^2**	**P-value**
[83]	RP = 0.48 MC + 5.50	0.998	3.7×10^{-5}	WV = -0.43 MC + 13.72	0.953	4.3×10^{-3}

[84]	RP = 0.48 MC + 5.50	0.994	1.7×10^{-4}	WV = -0.30 MC + 12.47	0.960	3.4×10^{-3}
[85]	RP = 0.70 MC + 4.60	0.991	3.9×10^{-4}	WV = -0.30 MC + 12.47	0.960	3.4×10^{-3}
[86]	RP = 0.76 MC + 4.4	0.994	1.7×10^{-4}	WV = -0.55 MC + 13.71	0.957	3.9×10^{-3}
Combined	RP = 0.64 MC + 4.82	0.964	1.7×10^{-14}	WV = -0.41 MC + 13.19	0.890	4.8×10^{-10}

555 RP: relative permittivity; MC: moisture content; WV: wave velocity.

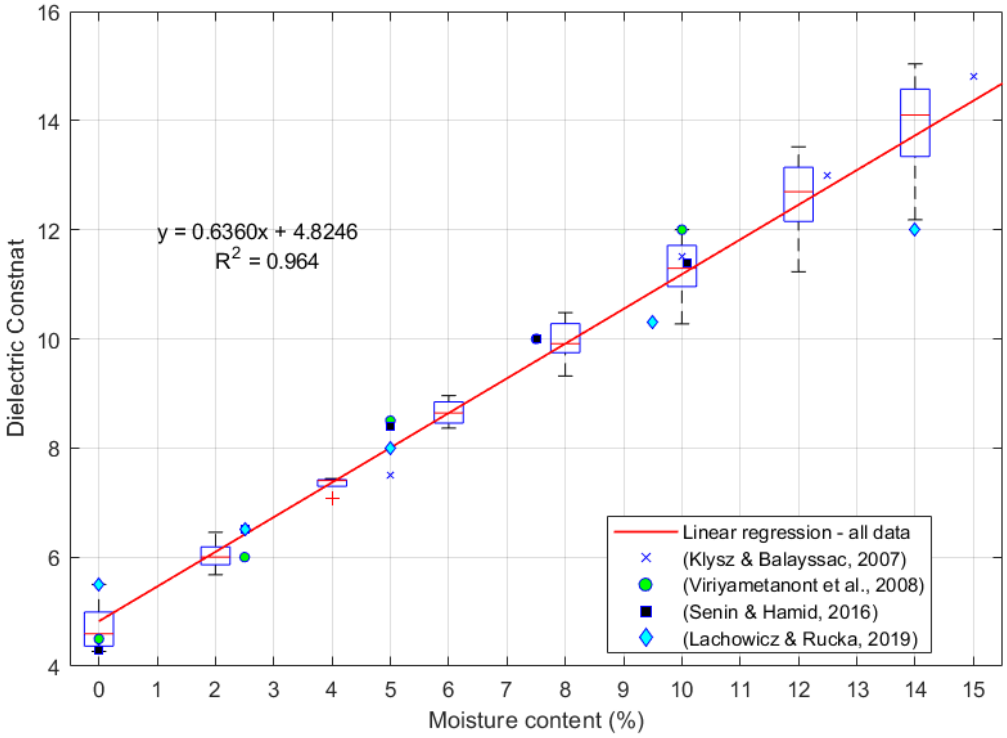

556

557 Fig. 16: Dielectric constant and moisture content linear relationship.

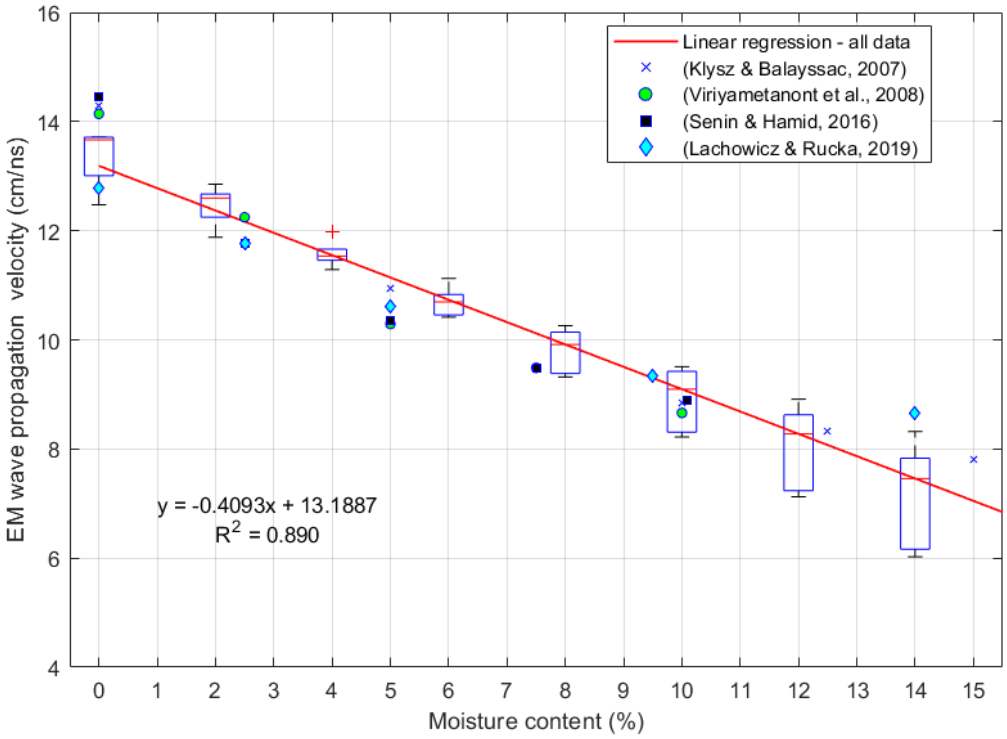

558

559 Fig. 17: EM wave propagation velocity and moisture content linear relationship.

560 Moisture content in concrete cover can also attenuate the RW and DW amplitudes collected
561 using ground-coupled GPR [82]. Table 12 summarizes the results of three experimental
562 research that studied the relationship between moisture content and attenuation level
563 [82,83,85]. The reviewed research studied concrete slabs with different moisture contents using
564 1.5 GHz GPR antennas. The reflection from the concrete slab surface (DW) and a steel sheet
565 reflector beneath the slab (RW) were recorded for further analysis. In these experiments, the
566 researchers used different slab thicknesses and different normalization equations. Therefore,
567 the normalization equations have been unified to be 20*Log(Ac/Adc), where Ac is the
568 amplitude of DW or RW and Adc is the amplitude of the direct wave from a calibration
569 concrete sample. In addition, as the researchers have used different slab thicknesses, the RW
570 attenuation was normalized using slab thickness to use the attenuation rate dB/cm for the
571 analysis. The extracted data were used to understand the attenuation of the waves with different
572 volumetric water contents.

Table 13 summarizes the statistical analysis of the relationship between the moisture content and the attenuation of the DW and RW. As shown in Table 13, the linear relationships established by the different studies are statistically significant, with p-values less than 0.05 and R^2 values exceeding 99% for all the regression models. Also, the regression model developed using all data to describe the relationships was found to be significant with small p-values (much lower than 0.05) and considerable R^2. Consequently, the null hypothesis can be confidently rejected, affirming the statistical significance of the established relationships.

Fig. 18 and Fig. 19 present the extracted data with linear regressions for a data set that combines the data extracted from all the studies. Also, box plots were utilized to compare the outcomes of regressions established by the three studies with those created using the combined dataset. Accordingly, the experiments' results in Fig. 18 illustrate a linear relationship between moisture content and DW attenuation. Similarly, Fig. 19 shows a representative linear relationship between volumetric moisture content and RW attenuation rate. The box plots show that deviations between the attenuation predicted by three studies progressively escalate as the volumetric water content increases.

Table 12: Moisture content effect on GPR signals amplitudes.

Reference	**Moisture content (%)**	**RW attenuation**	**DW attenuation**	**Normalization equation**	**Cover thickness (mm)**
[82]	[0,…,16]	[0,...,10.3]	[0,...,7.1]	20*Log(Ac/Adc)	80
[83]	[0,…,10]	[0.9,…,10]	(0,…,3]	20*Log(Ac/Adc)	120
[85]	[0,…,10.1]	[0,…, 9]	[0,…, 7]	20/d * log(Ac/Adc)	70

Table 13: Summary of the statistical analysis of the relationship between moisture content effect on GPR signals amplitudes.

Reference	**Moisture content % vs. RW attenuation**			**Moisture content % vs. DW attenuation**		
	Equation	**R^2**	**P-value**	**Equation**	**R^2**	**P-value**

[82]	RWA = 0.30 MC + 0.1	0.994	2.1×10^{-4}	DWA = 0.08 MC – 0.03	0.998	4.3×10^{-5}
[83]	RWA = 0.43 MC + 0.18	0.990	4.4×10^{-4}	DWA = 0.08 MC + 0.06	0.995	1.7×10^{-4}
[85]	RWA = 0.70 MC + 0.12	0.998	4.0×10^{-5}	DWA = 0.13 MC + 0.02	0.999	1.9×10^{-5}
Combined	RWA = 0.45 MC – 0.25	0.795	8.0×10^{-6}	DWA = 0.08 MC + 0.07	0.859	6.8×10^{-7}

592 RWA: RA attenuation per cm (db/cm); DWA: DW attenuation (db); MC: moisture content.

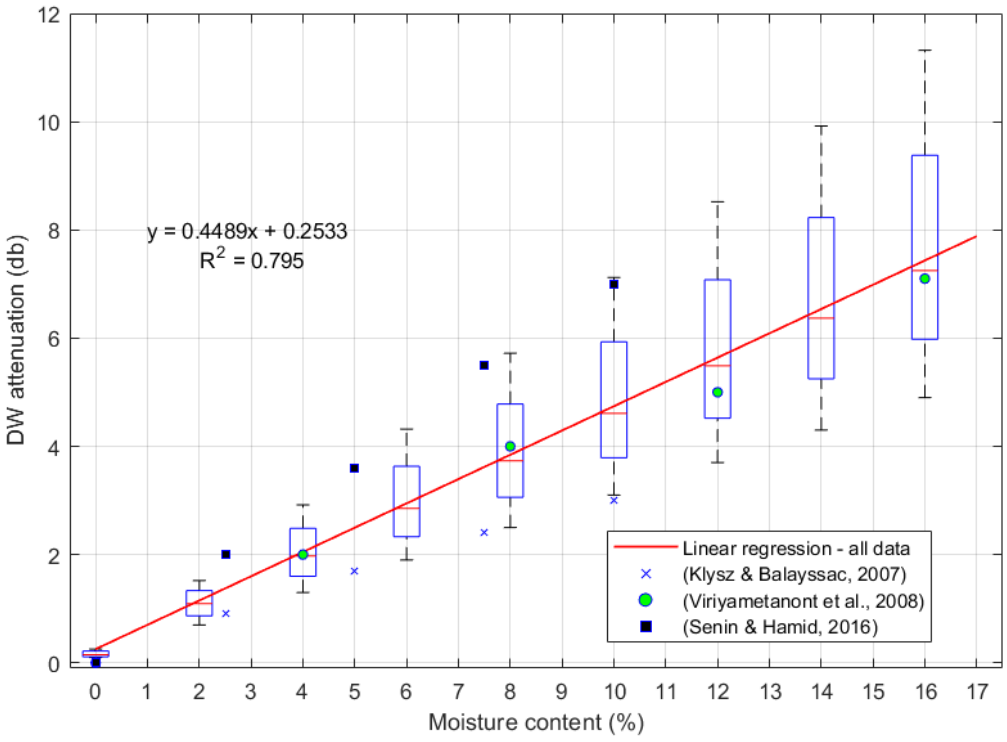

593

594 Fig. 18: DW attenuation and moisture content linear relationship.

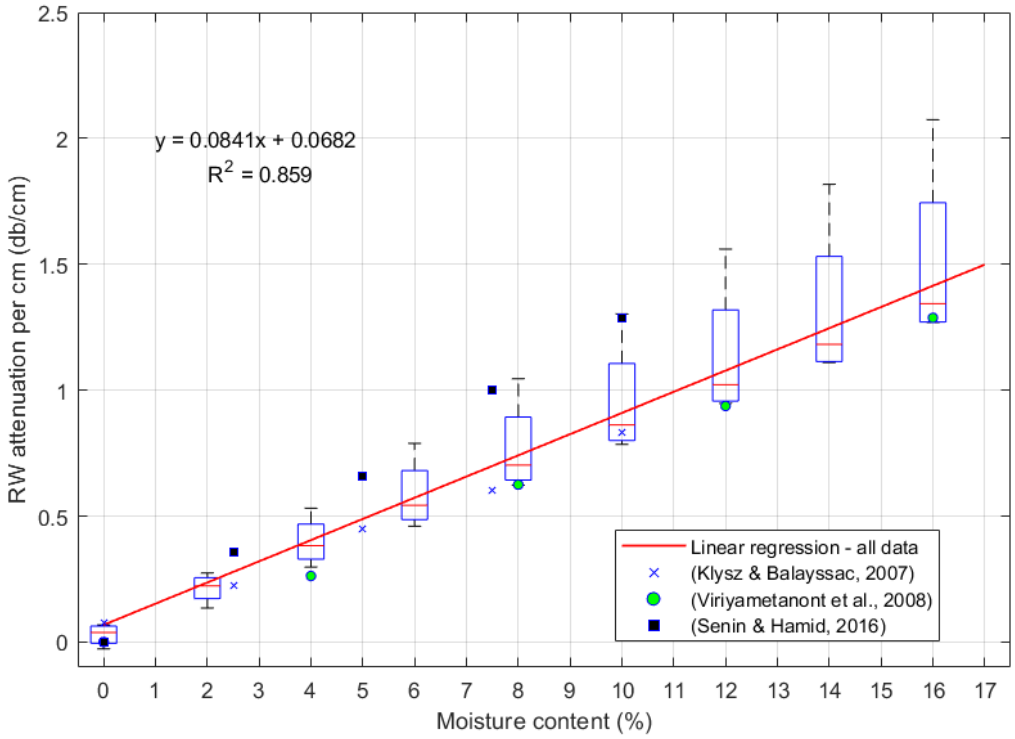

595

596 Fig. 19: RW attenuation rate and moisture content linear relationship.

597 *Chloride contamination effect on GPR signals:*

598 Chloride contamination has a significant effect on EM wave behavior in concrete [88]. The
599 reviewed literature studied the effect of chloride ions in time and time-frequency domains. The
600 time domain analyses the changes in the amplitudes and travel time of RW and DW, while the
601 time-frequency domain analyses the changes in the amplitudes and central peak frequencies of
602 RW and DW. In the time domain, multiple experimental research focused on the relationship
603 between chloride contamination and amplitude attenuation [82,85,89], and the results
604 demonstrate that chloride content can significantly affect concrete conductivity, particularly
605 with the presence of free chloride ions. Conductivity mainly influences the imaginary parts of
606 effective permittivity, which dominate energy loss and signal attenuation. On the same note,
607 chloride was found to be ineffective in dry concrete as chloride ions need moisture to be free.
608 Thus, the combination of chloride and moisture correlates with amplitude attenuation. Senin
609 and Hamid [85] conducted comprehensive experimental research to study the EM wave

behavior in concrete slabs under controllable moisture and chloride contamination levels by monitoring EM wave attenuation. According to the results summarised in Fig. 20, the DW attenuation is mainly affected by moisture content in the concrete cover, while free chloride content dominates the attenuation of the RW. Accordingly, the moisture content and chloride contaminant level in concrete structures can be estimated based on a comprehensive analysis of GPR wave attenuation. In this regard, multiple researchers [66,86,90,91] simulated the GPR using computer software to correlate the values of real (ε_r') and imaginary (ε_r'') parts of the relative permittivity (ε_r) with GPR wave attenuation and TWTT. The result was promising in terms of moisture and chloride mapping using the propagation velocity and attenuation of the RW and DW.

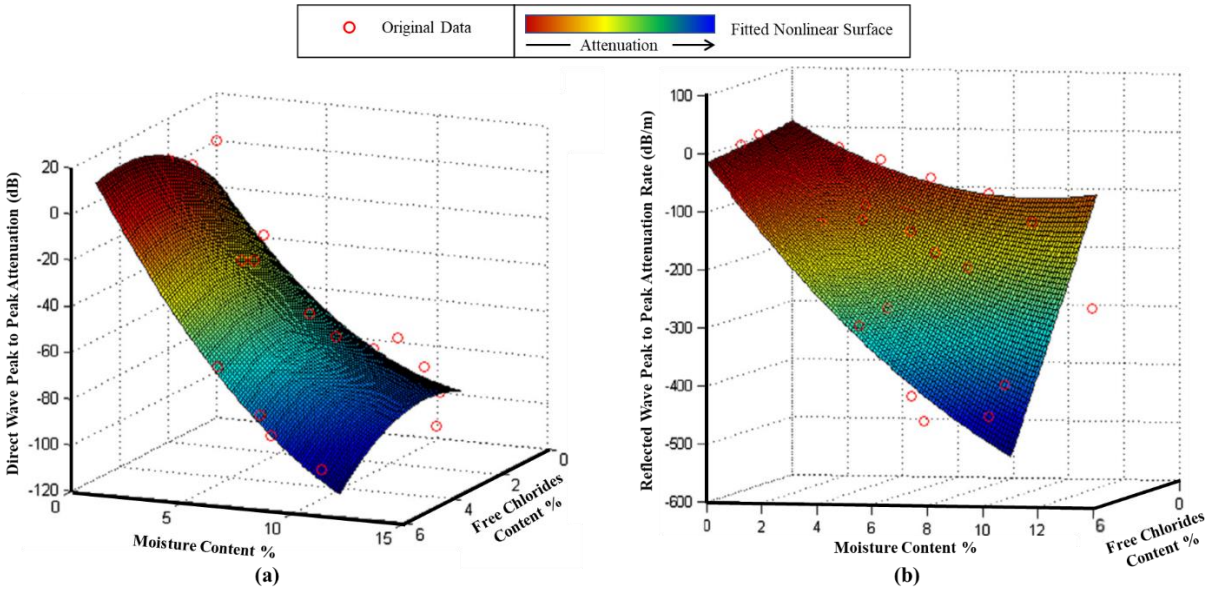

Fig. 20: (a) DW attenuation model and (b) RW attenuation model for varying free chloride and moisture content [85].

In the time-frequency domain, chloride contamination appears to have attenuation effects on the central frequency of RW and DW. Central wave frequency attenuation is usually studied using S-transformation, which is a method to transform the time domain into the time-frequency domain. Multiple scholars [91–95] have studied the effect of chloride concentration in the time-frequency domain. The results indicate that high moisture and chloride

628 contamination reduces DW and RW peak frequency and amplitude. Additionally, as the
629 moisture content decreases, the amplitude of the frequency spectrum increases while frequency
630 is slightly decreased. Accordingly, the peak frequency appears to be dependent on chloride
631 content. Therefore, the mapping of the DW peak frequency can be used to evaluate the
632 distribution of chloride contamination in concrete cover.

633 *Corrosion effect on GPR signals*

634 Corrosion is a chemical process in which steel reacts with oxygen and moisture to produce rust
635 on the metallic surface. The Corrosion process is accelerated in the presence of chloride ions.
636 Consequently, corrosion byproducts are usually accompanied by moisture and chloride ions.
637 To simulate the corrosion process, the researchers in Table 14 mainly applied accelerated
638 corrosion to deteriorate reinforced concrete specimens. However, the researchers did not
639 comprehensively discuss the distinct attenuation mechanism of the various affecting factors.
640 Thus, the overall effect of corrosion on GPR waves reveals conflicting outcomes based on the
641 variation of experimental setups.

642 The effect of corrosion on GPR waves has been investigated using a range of experimental
643 setups, as outlined in Table 14. In the first set of experiments, researchers [92,93,95,96]
644 immersed the reinforced concrete specimens in a saline solution for several days. Then, the
645 specimens underwent accelerated corrosion using induced current days after reducing the water
646 below the rebars' level. Subsequently, the concrete specimens were completely dried before
647 being scanned by a GPR antenna to eliminate the moisture effect. The GPR scans were
648 analyzed in time and time-frequency domains. The results indicate that the RW amplitude
649 increased while the TWTT decreased, and there was no significant change in the reflected wave
650 frequency. The authors attributed this to the additional reflections from the corrosion-concrete
651 interface that moved upward through cracks and pores near the surface. Furthermore, the

migration of chloride ions toward the reinforcement during the accelerated corrosion reduced their concentration in the concrete cover.

In the second set of accelerated corrosion experiments, Hong et al. [92] made an experiment similar to the ones in the first set. However, in this experiment, the concrete was fully dried after being submerged in a saline solution for a few days. Then, accelerated corrosion was applied directly to the dry specimen. The GPR scan outcomes were similar to the first setup, but it was noticeable that the cracks developed much earlier than in the wet environment. This was attributed to the localization of corrosion products near the reinforcement layer as fewer corrosion products migrated through concrete pores. On the same note, Hong et al. [94] used the same methodology, but instead of using saline solution, the chlorides were induced into the concrete mix before casting. The results were similar, with increased RW amplitude and concentrated corrosion products near the rebar interface.

In the third set of experiments, Tesic et al. [79] and Zaki et al. [28] accelerated the corrosion by applying direct current while the specimens were fully submersed in the saline solution. Following the corrosion process, the specimens were directly scanned with GPR without being dried. The outcomes of these experiments revealed a decrease in the RW amplitude and B-scans' sharpness. Conversely, there was an increase in the TWTT. The researchers attributed these changes to the simultaneous presence of chloride ions and moisture in the concrete cover.

In the fourth set of accelerated corrosion experiments, the rebars were corroded and cleaned before being embedded in a concrete or concrete-like oil medium [68,71,72]. The rebars have experienced different levels of mass loss, and the amplitude attenuation and B-scans blurriness exhibited a direct proportion to the percentage of mass loss. The authors mainly attribute this to the reduction of rebar diameter and the diminished backscattered energy due to the

irregularities on the corroded surface. However, this experimental setup is unrealistic as it misrepresents the effect of corrosion by-product migration through concrete pores.

Other exceptional experiments have been undertaken to tackle the complexity of the corrosion process effect on the EM waves. For instance, Sossa et al. [72] conducted a long-term corrosion simulation wherein reinforced concrete specimens were exposed to a humid environment for a duration of twelve months. The corrosion in this experiment occurred naturally and closely resembled the actual corrosion process. Examining the concrete specimen using GPR revealed a distinct reduction in RW amplitude and B-scans sharpness and an increase in TWTT. The authors attributed these observations to the influence of moisture and chloride ions contamination. On the other hand, Hong et al. [78] have used numerical simulation to mimic corrosion by-product migration through concrete cracks. The outcomes of this simulation indicate that filling vertical cracks with corrosion products increases the RW amplitude as it increases the reflecting ability of the rebar concrete interface.

Based on the preceding observations, it can be concluded that corrosion has complex effects on EM wave behavior. Thus, employing various experimental configurations caused a counteraction in interpreting the overall impact of corrosion on GPR scans. However, the systematic literature analysis managed to comprehend the effect of corrosion by dissecting the influence of each affecting factor. Accordingly, the existence of cracks and pores filled with corrosion by-products appears to increase the RW amplitude and decrease the TWTT. This outcome can primarily be attributed to the enhanced reflectivity arising from the migration of corrosion products toward the surface, creating multiple reflective layers. On the other hand, the simultaneous presence of moisture and chloride in the concrete cover reduces both RW amplitude and B-scans sharpness and increases the TWTT. However, the migration of chloride ions toward the reinforcement interface during the dry accelerated corrosion isolates the moisture and chloride effect on the permittivity and conductivity of the concrete cover. Finally,

the corrosion of reinforcement bars and reducing their mass prior to concrete casting reduces the reinforcement's ability to reflect the EM waves. However, this setup is unrealistic and misrepresents the complexity of the corrosion process.

Table 14: Effect of corrosion products on GPR signal.

Reference	Freq.	Domain	Experimental setup	Results[1]
[93][95]	1.5 GHz	Time & frequency	Experimental set 1: RC submerged in NaCl solution. Then, it underwent accelerated corrosion using induced current days after reducing the water below the rebars' level. The specimen was dried before GPR scans.	-RW amplitude increased. -TWTT decreased. -Frequency didn't change. -Corrosion products migrated to concrete pores.
[92]	2.6 GHz	Time & frequency		
[96]	2 GHz	Time		
[79]	2.7 GHz	Time		
[92][94]	2.6 GHz	Time & frequency	Experimental set 2: RC was submerged in NaCl solution [92], or chlorides were added to the concrete mix [94]. Then, accelerated corrosion using induced current was applied to dry concrete.	-RW amplitude increased. -TWTT decreased. -Frequency didn't change. -Fewer corrosion products migrated to concrete pores.
[28]	2.0 GHz	Time	Experimental set 3: RC submerged in NaCl solution. Then, accelerated corrosion is applied while the concrete is fully submerged in NaCl solution. The specimen was wet during GPR scan.	-RW amplitude decreased. -TWTT increased. -B-scans sharpness decreased.
[68]	2.6 GHz	Time	Experimental set 4: Rebars corroded outside and cleaned before concrete casting.	-RW amplitude decreased. -TWTT increased. -B-scans sharpness decreased with the mass loss.
[71][72]	1.6 GHz	Time		
[72]	1.6 GHz	Time	Reinforced concrete specimen embedded in a 95% humid area for 12 months.	-RW amplitude attenuation. -TWTT increased. -B-scans sharpness decreased.
[78]	2 GHz	Time	Numerical simulation for concrete cracks and corrosion by-products.	-The presence of cracks filled with corrosion by-products increases the rebar's reflecting ability, and so the RW amplitude.

[1]Observations in the corroded specimens compared to reference.

4.2.4 Other influential factors

The revised literature encompasses some factors with a limited effect on GPR interpretation results. These factors include environmental variables like temperature and relative humidity parameters. In this regard, Nguyen et al. [97] employed a deep belief network (DBN) to investigate the effect of various environmental factors on GPR results. Their study revealed

that temperature has a more significant influence than relative humidity. Similarly, Zatar et al. [98] used Artificial Neural Network (ANN) to study the effect of temperature, chloride contamination level, and ambient humidity on the reflected amplitude. The temperature and chloride contamination were found to have a significant influence on the amplitude attenuation compared to the relative humidity. Other factors, including supporting structures such as main girders, columns, beams, or any previous repairs, have the potential to introduce misinterpretations in the numerical analysis of GPR data [99].

4.3 GPR Analysis Methods

GPR data can be interpreted using various methods, and each method has its own merits and admires. As depicted in Fig. 21, the majority of these analysis techniques are centered around A-scan data. This section provides a comprehensive overview of these interpretation methods through an extensive and systematic review.

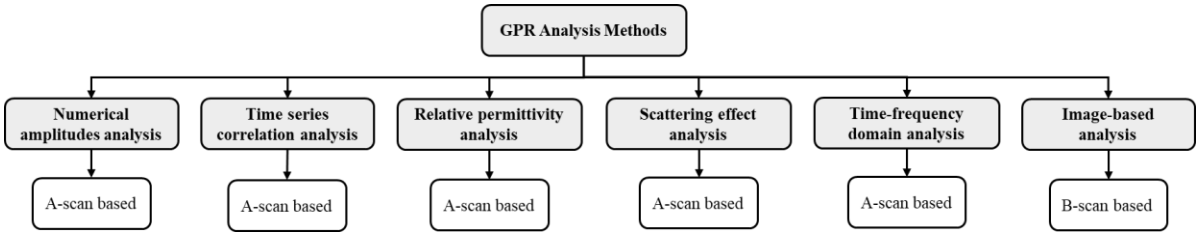

Fig. 21: GPR analysis methods.

4.3.1 Numerical amplitudes analysis

Numerical amplitude analysis is a quantitative interpretation method of GPR data that deals with amplitude and travel time values extracted from the A-scans. Numerical analysis has emerged as the predominant method for interpreting GPR data, primarily due to two main reasons. First, it accelerates data processing and reduces computational expenses compared to the visual analysis of B-scans. Secondly, the method is valued for its objectivity compared to the B-scan image interpretation, which relies heavily on the subjective judgment of experts [14]. However, the numerical interpretation method can lead to deceptive results due to the complexity of factors affecting the A-scans variables, as illustrated in the previous chapter. As

depicted in Fig. 22, the numerical analysis method is a comprehensive process that involves (1) data collection from the concrete decks using a horn or ground-coupled antenna, (2) data pre-processing, (3) amplitudes extraction, (4) amplitudes normalization, (5) depth correction, (6) thresholds selection for corrosion mapping, and (7) result's validation using ground truth or other NDT.

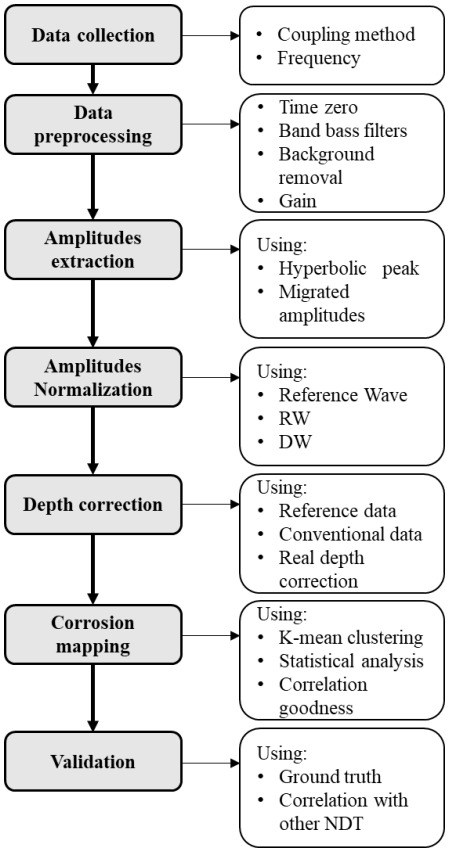

Fig. 22 Numerical amplitude analysis.

Data collection:

GPR data can be acquired using air-coupled (horn) or ground-coupled antennas. Horn antennas are usually attached to a moving vehicle, allowing for rapid data collection without disrupting traffic flow. According to the reviewed literature, this method is preferable for extensive studies that involve inspecting multiple bridges to conduct relative assessments. Statistical methods are commonly employed to interpret the data collected through this approach. On the contrary,

Ground-coupled antennas are more common for detailed bridge inspection, as 90% of the references in

Table 15 use ground antennas for data collection. The ground-coupled system is usually attached to a pushing cart that is manually dragged as it requires direct contact with the inspected surface. Some researchers have developed autonomous data collection systems that utilize autonomous robots to integrate GPR with other NDTs [26,59,100]. Autonomous data collection reduces workforce requirements and enables more robust data collection.

Besides the coupling system, the antenna frequency is also a critical aspect of GPR data collection. Based on the information compiled in

Table 15, 1 GHz is the most commonly used frequency for horn antennas. In comparison, the frequency range for ground-coupled antennas falls between 1.5 and 2.6 GHz, with 1.5 GHz being the most used frequency.

Table 15: Data collection in numerical-based analysis.

Ref.	Type	Overlay	Frequency	GPR setup
[101]	Field[1]	Asphalt overlay	2 GHZ	Ground
[102]	Field	Asphalt overlay	2 GHz	Ground dual polarization
[103]	Field	Bare concrete	1.5 GHz	Ground
[75]	Field	Bare concrete	1.5 GHz	Ground
[17]	Field	Bare concrete	1.5 GHz	Ground
[104]	Field	Asphalt and bare concrete	1.5 GHz	Ground
[59]	Field	Asphalt overlay	1.5 GHz	Ground by a robotic system
[76]	Field	Bare concrete	1 GHz	Air 4 channels
[105]	Field	Bare concrete	1.5 GHz	Ground
[106]	Field and laboratory	Bare concrete	1.5 GHz	Ground
[100]	Field	Bare concrete	1.5 GHz	Ground by a robotic system
[26]	Field	Bare concrete	1.5 GHz	Ground by a robotic system
[107]	Field	Seven overlayers types	1.5 GHz	Ground
[57]	Field	Asphalt overlay	1.6 GHz	Ground
[108]	Field	Bare concrete	1.5 GHz	Ground
[109]	Field	Bare concrete	2.6 GHz	Ground
[56]	Field	Bare concrete	1 GHz	Air 4 channels
[10]	Field	Asphalt overlay	1 GHz	Air 4 channels

[110]	Field and numerical simulation	Bare concrete	1.5 GHz	Ground
[15]	Field and laboratory	Bare concrete	1 GHz air & 2.6 GHz ground	Ground and Air
[111]	Field, laboratory, and numerical simulation	Asphalt overlay	1.5 GHz	Ground

[1]Field means bridge deck

Data preprocessing:

Following data collection, the pre-processing of the raw signals is necessary to prepare the data for subsequent analysis. In the revised literature, signal pre-processing encompasses time-zero correction and band-pass filtering. Other pre-processing techniques, such as background removal and gain, are not recommended as they can affect the numerical values of the extracted amplitudes. In time zero correction, the gap between the antenna and the scanned surface is eliminated to uniform the starting points of the received signals and exclude the effect of inhomogeneity of the survey path. Thus, after time zero correction, the travel time to the inspected surface is equal to zero [15].

GPR signals may interfere with other undesirable radio waves in the surrounding environment. Thus, the noises from the surrounding environment should be detached to enhance the interpretation quality. To isolate the induced noise, two types of band filters are employed: Infinite Impulse Response (IIR) and Finite Impulse Response (FIR) filters. While both filters work similarly, FIR is generally preferred due to its stability, as IIR filters might alter the waveform shape and introduce slight phase shifts in the data [112]. In this regard, Low and High-pass filters are commonly used to eliminate the signals with undesirable frequencies. The low-pass filter excludes the undesirable high-frequency components of the data. On the contrary, the high-pass filter eliminates the noisy low-frequency bands. The range between low and high-pass filters should be optimized to reduce the noise without causing loss of useful data. Cassidy [30] and Hashim et al. [113] suggested that the pass region should be symmetric

around the GPR central frequency with a bandwidth equal to 1.5 the nominal frequency. For instance, if the nominal frequency of the antenna is 2 GHz, the band bass is recommended to be between 0.5-3.5 GHz.

Amplitudes extraction:

The numerical analysis of GPR data starts with picking up the rebar location to extract amplitude and two-way travel time (TWTT) information. As indicated in Table 17, some references have identified the vertex of the hyperbolic shapes as the precise location of reinforcement rebars. Accordingly, the reflection amplitude at the vertex of the hyperbolic shapes is manually or automatically picked from the radargram. However, it has been observed that the peak amplitude of rebar reflection does not always occur at the hyperbola vertex. Thus, ASTM D6087 [114] suggested the use of migration to improve the robustness of rebar localization and amplitude extraction [15,107,108].

Migration involves transforming the unfocused space-time GPR B-scan into a focused image where the hyperbolic shapes are concentrated near the parabolic vertex, as shown in Fig. 23. Özdemir et al. [115] studied the migration algorithms performance based on their processing time and migration quality. Namely, Kirchhoff migration, Stolt migration algorithm(ω-*k*), hyperbolic summation, projection-based migration, and phase-shift migration algorithms have been examined and evaluated. Among the tested algorithms, the Stolt migration (ω-*k*) outperformed other algorithms in terms of processing time and migration quality. On the same note, Wei and Zhang [116] studied the evaluation metrics for migration performance and found that migration achieves the best performance when the migration velocity is close to the average EM wave propagation velocity. In more detail, the hyperbolics will be under-migrated if the migration velocity is less than the propagation velocity and over-migrated if the migration velocity exceeds the wave propagation velocity.

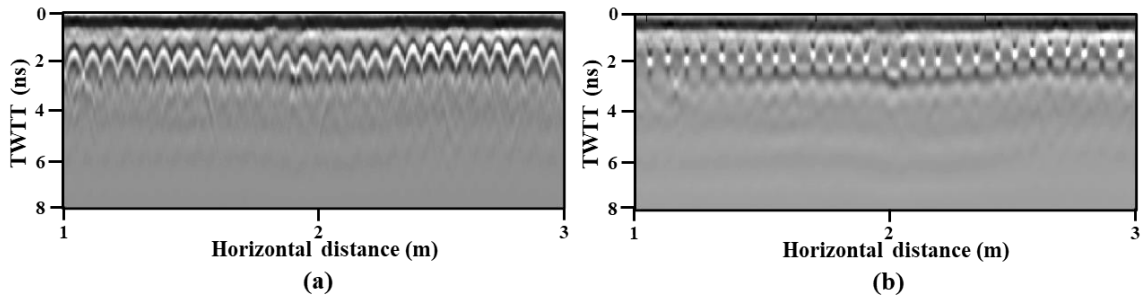

Fig. 23: GPR signal (a) before migration and (b) after migration.

Amplitudes normalization:

After extracting the amplitude and TWTT data, it is essential to normalize the amplitudes before conducting the numerical analysis. As shown in Table 17, the reviewed literature used different normalization methods. For instance, as shown in Eq. (7), Barnes et al. [17] used the highest 10% RW amplitude to normalize other amplitude. Similarly, [26,100,103,104] followed the same normalization method and used Eq. (7). On the same note, Dinh et al. [75] have used the average direct coupling to normalize the RW, as shown in Eq. (8). This normalization method is preferable for data from multiple concrete bridges as it minimizes the effects of irregular direct coupling [75]. In addition, some references used the DWs to normalize their corresponding RWs, as shown in Eq. (9). This normalization method reduces the effect of surface irregularities like patches or potholes [108]. Few researchers used the reflected waveform from a steel plate to normalize the RW and DW amplitudes as shown in Eq. (10). In addition, Eq. (11) uses the real depth to normalize the amplitudes and estimate the attenuation rate. Finally, Eq. (13) uses the RW and DW subtraction for normalization, and it was rarely used in the reviewed literature.

$$A(dB) = 20 * \log\left(\frac{RW}{max10\%\ RW}\right) \tag{7}$$

$$A(dB) = 20 * \log\left(\frac{RW}{Avg\ DW}\right) \tag{8}$$

$$A(dB) = 20 * \log\left(\frac{RW}{DW}\right) \quad (9)$$

$$A(dB) = 20 * \log\left(\frac{RW}{Steel\ sheet\ reflection}\right) \quad (10)$$

$$A(dB/cm) = 20 * \log\left(\frac{RW}{DW * cover\ depth}\right) \quad (11)$$

$$A(dB) = \left(\frac{RW}{maxRW}\right) \quad (12)$$

$$A(dB) = 20 * \log(DW - RW) \quad (13)$$

Depth correction:

The variations in concrete cover thickness can significantly affect the attenuation of GPR signals, as deeper rebars exhibit higher attenuation rates [75]. Therefore, depth correction is essential to mitigate the effect of cover depth variations on amplitude values. The ideal depth correction can be achieved by establishing a regression between normalized amplitudes and true rebar depth. However, the rebar depth estimation is complex as the concrete cover may have substantial variations in permittivity and conductivity values. Table 16 provides an overview of the existing research endeavors concerning the accurate estimation of concrete cover depth. For instance, Pashoutani and Zhu [110] used migration along with evaluation metrics to estimate the EM waves' propagation velocity corresponding to the optimal migration performance. The estimated velocity was subsequently incorporated with TWTT to estimate the depth of the reinforcement bars. In addition to migration, the hyperbolic signature of the rebars has commonly been utilized to estimate their depth and size using curve-fitting techniques [67,117,118]. This approach has been demonstrated to be effective in accurately estimating the reinforcement depth. However, this estimation method is still complex and computationally expensive. In addition, the modifications made by Zhou et al. [69] and Agred et al. [67] to the GPR device have escalated the cost and technical complexity of the procedure. Consequently, most researchers utilized the TWTT to formulate the regression with normalized

amplitudes, assuming that any bridge deck will have sound concrete portions exhibiting the least amplitude attenuation at specific TWTT intervals.

Table 16: Concrete cover depth estimation methods.

Reference	Freq	Processing method	Antenna Modification	Accuracy	Type
[117]	1.5 GHz	Pattern recognition and curve-fitting	No	6.73% for cover depth and 6.19% for sizes	Shear wall
[118]	1.5 GHz	Hyperbolic signatures model	No	3.12% for cover depth	Sand simulation tank
[69]	-	GPR and electromagnetic induction (EMI) methods	Dowel GPR and EMI sensors	5% for cover depth 6.7% for size.	Newly constructed building
[67]	1.5 GHz	Hyperbolic signatures model	Double receiving antennas	2 mm for thickness of 15 to 80 mm	Laboratory concrete slap
[110]	1.5 GHz	Migration	No	-	Numerical simulation and concrete decks

As outlined in Table 17, several depth-correction methods have been devised based on the regression between TWTT and the 90th percentile amplitudes. For instance, Barnes et al. [17] used the 90th percentile amplitudes within TWTT intervals (usually 0.5 ns) containing a minimum of 30 amplitude measurements to develop a linear regression with TWTT. Subsequently, the linear regression formula is subtracted from the normalized amplitudes. On the same note, Dinh et al. [75] leveraged 23,587 data points from sound concrete parts of multiple concrete bridges to formulate a standardized linear regression equation with TWTT. Upon comparison with the conventional depth correction, Dinh et al. [75] observed that the conventional depth correction tends to overcorrect the amplitudes with high TWTT. Overall, the time-based depth correction outcomes emphasize its significant contribution to enhancing the accuracy of corrosion mapping. Recently, Deck and Pashoutani [110] applied a real depth correction after estimating the rebars' depth using migration at different velocities; the findings indicate that time-based depth correction underestimates the deterioration level of concrete decks at certain locations.

Corrosion mapping:

Corrosion mapping is the most critical part of the GPR data interpretation process. In this stage, the analysts determine the number of condition categories and allocate thresholds to cluster the processed amplitudes. The clustered amplitudes are then mapped to create a visual representation of the concrete condition. The mapping results are usually compared with ground truth or other NDT to validate the interpretation results.

The number of condition categories and thresholding methods vary across the reviewed literature. The utilized methods mainly include unsupervised clustering techniques, correlation with other NDT, and statistical analysis of the normalized amplitudes. In addition, some papers use continuous color scales to highlight the law amplitude areas without defining thresholds or condition categories [26,59,75,100,119]. However, this scale is not practical for conducting condition assessments, especially when comparing the state of multiple structures.

Unsupervised clustering algorithms have been commonly utilized to draw the thresholds between different condition categories. In practice, the analyst has to specify the number of clusters, usually three or four, and the unsupervised algorithms estimate the threshold values [57,102,106]. In a comparative study, Ata et al. [102] compared various unsupervised clustering techniques. The study revealed that K-means, the most commonly used clustering method, outperformed the other methods by providing more compact clusters and better-separated points. However, the unsupervised clustering proved to be unreliable and often indicates severe corrosion percentages even in newly constructed slabs. To tackle this concern, Alsharqawi et al. [120] and Mohammed Abdelkader et al. [121] systematically analyzed the thresholds derived from applying unsupervised clustering techniques to multiple bridges, aiming to refine and optimize standardized thresholds. However, the standardized thresholds may not be applicable when there is substantial variation in the physical properties, such as cover depth [17]. In another study, Dinh et al. [104] developed an algorithm that determines

the number of K-mean clusters based on the overall condition and age of the concrete bridges. Accordingly, the number of clusters will be two for the newly constructed bridges and increase to three or four for old and deteriorated bridges. Yet, this clustering method still identifies deterioration even in brand-new slabs, and the threshold values vary significantly from one structure to another. These limitations render these clustering techniques unreliable and unsuitable for large-scale studies that require a comparative assessment of structural conditions.

Another way for GPR condition mapping is to use the goodness of correlation with other techniques, such as HCP and chain drag, to find the optimum threshold for active corrosion identification [10,15,17,26,103,110]. This method aims to find a standardized threshold that can separate deteriorated areas from sound areas. Gucunski et al. [26] examined the obtained threshold's repeatability on the same bridge deck over five years, revealing an 86.4% average agreement in deteriorated areas between previous and later surveys. Similarly, Barnes et al. [17] tested the standardized threshold on diverse concrete bridges, revealing that substantial differences in mean cover depth influence the threshold values. Hence, assigning crisp values for the thresholds may introduce uncertainty in the mapping of concrete conditions.

Furthermore, other researchers [15,56,76,107–109] applied a statistical analysis on the normalized amplitude values to use statistical properties such as mean, median, skewness, and standard deviation for threshold estimation. After monitoring the effect of corrosion progression on the normalized amplitudes' distribution, Sun et al. [107] noted that rebar corrosion shifts the amplitude distribution towards the negative side. Similarly, Maser et al. [15] observed that as deterioration advances, the standard deviation and the skewness significantly increase. Optimizing these statistical parameters through alignment with other non-destructive testing (NDT) technologies could potentially yield reliable thresholding results [76].

Following the evaluation of the concrete structure's condition, the analysts are required to present the data and ensure seamless rectification of the destresses. Thus, the condition map must be linked with precise X and Y coordinates [64]. The conventional approach for presenting the interpretation results involves visualizing the data on a heat map, with different colors corresponding to each condition category. The heat map can then be projected onto a 2-D, or onto a 3-D representation by employing interpolation techniques between the migrated B-scans [101]. For 3-D representation, efficient processing methods are required to filter out the background noise from the B-scans. In this regard, Feng et al. [122] introduced a learning-based GPR data analysis method, encompassing a noise removal module and a Convolutional Recurrent Neural Network (CRNN) to estimate the dielectric value of the subsurface medium in the B-scans. In addition, Dinh et al. [11] utilized a dual-polarized antenna to provide a comprehensive high-resolution 3D representation of the concrete. Furthermore, Kilic and Caner [123] utilized augmented reality to integrate the condition map obtained from GPR with other NDTs. For GPR analysis, Kilic and Caner [123] used a 2 GHz antenna to collect high-resolution data and utilized K2 Fast-Wave and IDS GRED software to receive, monitor, and analyze the collected data before constructing the 3D and 2D representations of the survey area.

GPR manufacturers have started incorporating 3D imaging and augmented reality features into their systems to enhance the visualization and interpretation of GPR data. For instance, Guideline Geo [43] has introduced the MALÅ MIRA (3D Imaging Radar Array) system that integrates multiple antennas with MALÅ ProEx control unit where up to 30 antennas can simultaneously gather data in real-time. The system promises to rapidly collect full 3D data to be displayed, interpreted, and exported into suitable GIS or CAD data formats. Similarly, Ingegneria Dei Sistemi (IDS) [39] developed a comprehensive system based on the Opera Duo and DS2000 GPR to track the radar's position and automatically mark the targets. Subsequently, the acquired data can be exported to CAD and GIS, and reports can be produced

directly on-site. However, this system was mainly designed for unparalleled utility locating and mapping. Furthermore, Proceq [42] has developed the Subsurface Mapping GPR systems (GP8800, GP8000, and GP8100) to provide a real-time image of the underground in 2D, 3D, and Augmented Reality. Similarly, Geophysical Survey System Inc. (GSSI) [38] developed the StructureScan Mini with an Augmented Reality option to provide real-time visualization for concrete inspection applications.

939 Table 17: Numerical-based analysis.

Title	Amplitude extraction	Norma-lization	Depth correction	Thresholding and clustering	Validation
[102]	Hyperbolas peak	-	Conventional 90th percentile regression with TWTT	4 categories (K-means)	stress map (finite element model).
[103]	Migrated amplitude	-	Conventional 90th percentile regression with TWTT	Correlation with deterioration depth.	LiDAR mappings (deterioration depth).
[75]	Hyperbolas peak	Eq. (8)	Standardized 90th percentile regression between Sound concrete data and TWTT	Auto mapping	ER, HCP, & IE.
[17]	Migrated amplitude	Eq. (7)	Conventional 90th percentile regression with TWTT	2 categories based on correlation with chain and HCP.	Chain drag & HCP
[104]	Migrated amplitude	Eq. (7)	Conventional 90th percentile regression with TWTT	1 2 or 3 categories based on concrete condition (K mean)	ER, HCP, & chloride content
[59]	Hyperbolas peak	-	-	Auto (0-20)	IE, ER, & USW
[76]	Hyperbolas peak	(13)	Conventional 90th percentile regression with TWTT	-	Visual inspection
[106]	Hyperbolas peak	-	Conventional 90th percentile regression with TWTT	4 categories (K-means) & statistical analysis	Cores, HCP, & test on a brand-new bridge
[100]	-	-	-	-	-
[26]	Hyperbolas peak	Eq. (7)	-	Correlation with ER, HCP, and IE.	ER, IE & HCP.
[107]	Migrated amplitude	Eq. (8)	Standardized 90th percentile regression between Sound concrete data and TWTT	Statistical analysis (Median - 3*MAD threshold line)	Acoustic scanning
[57]	Hyperbolas peak	Eq. (7)	Conventional 90th percentile regression with TWTT	3 categories (k-means)	IRT
[108]	Migrated amplitude	Eq. (9)	Conventional 90th percentile regression with TWTT	2 categories are subjectively divided at (-dB)	Chain drag
[109]	Hyperbolas peak	(9)	Conventional 90th percentile regression with TWTT	correlation between HCP and (skewness*mean) of the normalized amplitude.	HCP
[56]	Hyperbolas peak	(10)	-	-	-
[10]	Hyperbolas peak	(10)	Conventional 90th percentile regression with TWTT	Correlation with deterioration depth & corrosion if the deterioration depth exceeded the clear cover.	Core samples, visual inspection, & chloride content
[110]	Hyperbolas peak	(11)	Real depth correction	1 category separated at 0.7dB/cm. Based on the correlation with chloride and HCP testing.	HCP & chloride content
[15]	Migrated amplitude	(12)	-	Correlation between HCP and GPR	Saw-cut, HCP & IE.
[120]	Migrated amplitude	Eq. (7)	Conventional 90th percentile regression with TWTT	4 categories standardized thresholds based on statistical analysis of multiple bridges.	HCP, & Cores
[121]	Migrated amplitude	Eq. (7)	Conventional 90th percentile regression with TWTT	4 categories standardized thresholds based on multi-objective optimization.	-

940

4.3.2 Time series correlation analysis

Numerical analysis of A-scan attributes is based on the relative difference in the reflections from different scans. However, this comparison can yield deceptive outcomes due to the variations in the factors influencing the reflections in different scans. Therefore, Dinh et al. [105] proposed the analysis of time-series GPR data as an alternative to the ordinary numerical amplitudes analysis. As outlined in Fig. 24, this analysis method observes the alterations in GPR signals collected for the same location at different points in time. This approach involves assessing the degree of similarity in the time series data. The degree of similarity is estimated by computing the correlation coefficients between the new and old (baseline) A-scans, assuming that higher similarity indicates a better condition. Accordingly, a contour map can be developed to present the distribution of the correlation coefficient. The map provides an overview of the concrete deck's condition, suggesting that a low correlation coefficient indicates potential corroded reinforcement.

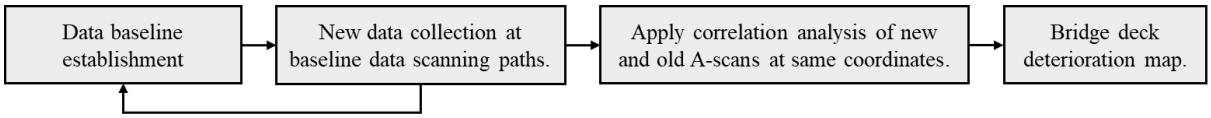

Fig. 24: Time-series correlation analysis methodology.

This interpretation method is more focused than the traditional numerical analysis. However, this method can lead to deceptive outcomes due to the potential variations in A-scan locations and the presence of multiple factors influencing scan shapes beyond corrosion. Furthermore, this method requires collecting and storing baseline data while the bridge is still in good condition. Consequently, this method is considered suitable for lifespan corrosion monitoring. Nevertheless, a meaningful classification of the correlation values is essential for this method to provide an effective condition assessment tool [105].

4.3.3 Relative permittivity analysis

As concrete ages in the presence of environmental deterioration factors, its porosity increases, and cracks develop due to repetitive strains in the concrete cover [56]. The porosity and surface cracks increase the concrete capacity to absorb water. Consequently, the presence of moisture exacerbates the concrete's deterioration, as numerous degradation mechanisms are linked to the presence of moisture. As highlighted in section 4.2.3, the relative permittivity and EM wave propagation velocity in the concrete medium are primarily influenced by its moisture content. Thus, the elevated permittivity values in concrete cover indicate potential deterioration [108].

In this regard, Agred et al. [67] developed an algorithm to estimate the EM wave propagation velocity in the concrete medium using GPR with dual receiving antennas. The propagation velocity was mapped to show the moisture distribution in the concrete cover and indicate the cover condition. On the same note, Rhee et al. [56] used the relative permittivity of concrete to evaluate the condition of bare concrete bridge decks. After surveying fifty-three concrete bridges, Rhee et al. [56] indicated that the aging factor reduces the concrete relative permittivity in dry conditions as the material tends to be more porous. Simultaneously, the high porosity increases the concrete's volumetric water capacity and elevates the relative permittivity in wet conditions. Thus, Rhee et al. [56] developed a threshold demonstrating the damage in concrete cover when the relative permittivity is higher than 11.0 or lower than 6.0. These two thresholds were established at the mean permittivity ± 1.5 standard deviations. This method can be a promising tool for mapping the condition of concrete cover and accurately identifying deteriorated areas.

4.3.4 Scattering effect analysis

Scattering refers to the phenomenon of electromagnetic waves being reflected or scattered by objects such as steel rebars. Rebars' scattering behavior is influenced by rebar diameter, rebar surface condition, and antenna polarization [60]. For instance, a rebar usually exhibits a

stronger reflection from a co-polarized antenna compared to a cross-polarized one [61]. Polarimetric technology is widely used in microwave remote sensing applications for terrain classification. The polarimetric GPR was introduced by Liu et al. [53] as an upgrade to the single-polarization GPR. This polarimetric approach has been employed to detect early-stage deterioration of reinforcement by analyzing the scattering patterns under different polarization modes.

To examine the scattering behavior of reinforcement rebars, Liu et al. [53] utilized a polarimetric GPR system to record rebar reflections in two orthogonal channels. Following preprocessing and migration of the recorded reflections, the H-Alpha decomposition technique was employed on the reconstructed GPR images. H-Alpha decomposition is a widely exploited process for categorizing targets' scattering mechanisms in polarimetric synthetic aperture radar (SAR) data. The primary objective of applying this method to GPR data was to classify the reinforcement bar's scattering characteristics at various corrosion stages. Accordingly, the full-polarimetric scattering matrix can be developed through polarimetric transformation and system calibration.

After examining the method on an accelerated corroded specimen, Liu et al. [53] observed a transformation in the scattering mechanism of the corroded rebar with the progress of the corrosion process. The scattering mechanism shifted from low-entropy dipole scattering to low-entropy surface scattering. This transformation demonstrates that the corrosion process affects the smoothness of the rebar surface and changes its scattering behavior. Accordingly, scattering characteristics can offer insights into initial reinforcement corrosion [53]. This approach requires further research to establish a criterion for the quantitative assessment of rebar corrosion and to comprehend the influence of moisture and chloride on the results.

4.3.5 Time-frequency domain analysis

The previously discussed analysis methods primarily analyze A-scan attributes within the time domain where the amplitude is presented versus travel time. However, in the time-frequency domain, A-scan amplitudes are presented versus time and frequency. The time-frequency domain offers insights into how the signal's frequency components change over time. As outlined in section 4.2.3, chloride contamination appeared to attenuate the central frequency of RW and DW. Frequency attenuation is commonly investigated using S-transformation, which is a method to transform the time domain into the time-frequency domain.

The simultaneous existence of chlorides and moisture accelerates the corrosion process. Thus, the early detection of chloride ion contamination can aid in the early detection of initial corrosion stages. In this regard, the researchers [90,92–95] studied the effect of chlorides and moisture content in the time-frequency domain. The results indicate that chloride ingress into the concrete cover attenuates the frequency of RW and DW in dry and moist environments. Accordingly, Hong et al. [92] mapped the chloride distribution based on the attenuation of DW peak frequency and used Laser-Induced Breakdown Spectroscopy (LIBS) to validate the mapping accuracy. On the same note, Hong et al. [94] integrated the mapping of amplitudes and frequency attenuation and suggested that areas with high amplitude and high frequency indicate severe corrosion, areas with low amplitude and low frequency indicate chloride contamination and possibly active corrosion, and areas with low amplitude and high frequency indicate sound concrete. This analysis method provides promising outcomes in terms of accurate corrosion assessment. However, the analysis is computationally demanding and requires further research to establish quantitative measures for assessing the corrosion condition.

4.3.6 Image-based analysis

GPR is primarily an imaging device. Therefore, the B-scan profile exhibits the most valuable parts of the information. Hence, solely analyzing numerical amplitude values disregards fundamental components of the GPR data [14]. In addition, relying solely on numerical analysis can lead to deceiving results due to the complexity of the affecting factors, such as surface anomalies, depth variation, and reinforcing bar configuration. These factors indicate that numerical analysis is not as efficient as visual analysis [99].

The image-based analysis primarily relies on the analyst's judgment to interpret the B-scan features into categorical conditions, as shown in Fig. 25. In this approach, the concrete condition is typically categorized into two or three categories. As illustrated in Table 18, the analyst, manually or with computer assistance, examines the B-scan features to establish condition boundaries based on predetermined evaluation criteria. The evaluation criteria are usually formulated based on the analyst's experience or based on the judgment of a group of experts via questionnaires [124]. The most frequently monitored B-scan features encompass blurriness, deformations in the reinforcement layer, changes or disappearance of slab boundaries, horizontal clutter caused by cracks and delamination, clarity of the second rebar layer, and the existence of structural features. Accordingly, the analyst can eliminate minor amplitude variations and unrelated anomalies, effectively enhancing the accuracy of the concrete's condition assessment. In addition, this method allows for precise differentiation of corrosion zones as the exact limit of corrosion zones can be mapped without the need for interpolation [14].

Overall, visual analysis of B-scans is considered a more thorough approach than numerical analysis [14]. Nonetheless, this approach is subjective as it heavily relies on the analyst’s judgment, which can lead to variations in the interpretation results. To address this concern, machine learning and computer vision technologies can be employed to automate the analysis

of B-scans by identifying key image features such as blurriness, hyperbolic shapes, reinforcement layer deformation, and slab boundary disappearance.

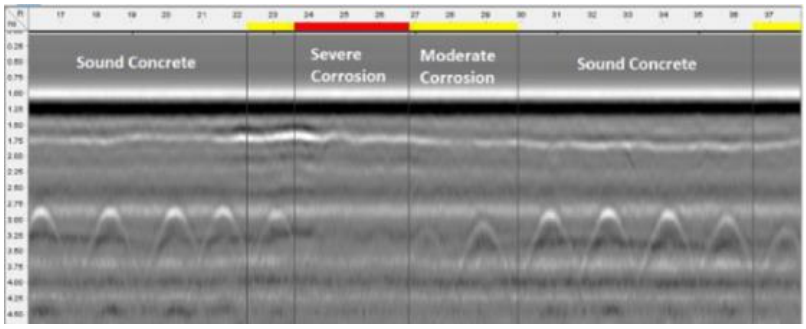

Fig. 25. B-scan analysis [99].

Table 18: Image-based analysis.

Ref.	Type	Overlay	Freq	Coupling	Assessment method	Number of categories[1]	Validation
[123]	Bridge deck	Asphalt	2 GHz	Ground	B-scan visualization based on self-identified rules	2	Integration NDT methods
[99]	Bridge deck	Asphalt	1.5 GHz	Ground	B-scan visualization based on self-identified rules	3	Cores & HCP.
[14]	Concrete slab	Bare	2 GHz	Ground	Computer-assisted B-scan visualization based on self-identified rules.	3	Cores & amplitudes analysis verification.
[125]	Bridge deck	Asphalt	1 GHz	Air	B-scan visualization based on self-identified rules	2	HCP and Chain Drag
[124]	Bridge deck	Asphalt	1.5 GHz	Ground	Computer-assisted B-scan visualization based on experts' identified rules.	3	Amplitudes analysis verification.
[126]	Bridge deck	Asphalt	2.6 GHz	Ground	B-scan visualization based on self-identified rules.	3	Chain Drag and concrete cover removal.
[127]	Bridge deck	Asphalt	2+1 GHz	Ground	B-scan visualization based on self-identified rules.	2	Wave velocity verification.
[128]	Bridge deck	Asphalt	2 GHz	Ground	B-scan visualization based on self-identified rules.	2	Amplitudes analysis verification.
[55]	Concrete tunnel	Bare	0.9 GHz	Ground	B-scan visualization based on self-identified rules.	3	Cores.

[1]Number of condition categories. It could be three (sound concrete, moderate corrosion, and severe corrosion) or two (sound concrete and corroded concrete)

4.4 Automated Rebar Recognition

The process of rebar recognition and amplitude extraction is notably time-consuming. Therefore, incorporating automated solutions into the rebar recognition process promises to

enhance efficiency and decrease the need for manual labor. Automated rebar detection in GPR images is a complex task due to various factors, such as low contrast, low signal-to-noise ratio, and complex field data. The detection of hyperbolic patterns is particularly challenging, which can have a significant impact on the accuracy of automated corrosion assessments. Several techniques, including thresholding, hyperbolic signature recognition, machine learning, and deep learning algorithms, have been employed to automate the process of rebar recognition.

4.4.1 Rebar recognition based on the hyperbolic signature

A specific avenue of research endeavors outlined in Table 19 focused on automating rebar detection using template selection and thresholding methods to recognize the hyperbolic signature in the B-scans. For instance, Wang et al. [129] utilized the templet matching method (SSD) to recognize the hyperbolic signatures. SSD is an algorithm that uses the sum of squared differences between a sliding temple and the target image to evaluate their similarity. Following rebar recognition, hyperbolic fitting was applied using partial differential equations to find the exact location of the apex. In a more recent study by Ma et al. [130], following the data preprocessing stage, the hyperbolic signature was identified using SSD. Subsequently, an adaptive hyperbolic fitting model was employed to pinpoint the hyperbolic apex. In another study, Dinh et al. [131] applied the limited and simplified hyperbolic summation (LSHS) migration algorithm on the time-corrected B-scan to condense the hyperbolic shapes into a reduced number of pixels. Accordingly, the model involved picking the pixels with positive values and refining them by applying a threshold to the number of positive cells in the migration path. Similarly, Xiang et al. [132] designed cascaded spatial frequency filters to decompose the rebar hyperbolas into tails with different directions. The decomposed hyperbola tails were set together to reconstruct the rebar hyperbolas using a proposed similarity score. Subsequently, curve fitting was used to identify the rebar signature in GPR data. In the same regard, Wang et al. [133] presented a semi-automatic approach for rebar detection that looks

into the best-fit hyperbolas in sub-windows at rebar locations and compares them with reflected signals of rebar according to similarity criteria. A rectangular sub-windows were created in the binary edge images, and the searching process for hyperbolic edges was addressed using a genetic algorithm (GA) and hyperbola matching analysis based on the time-distance relationship of reflections.

Thresholding and template matching have been adopted to automatically extract the rebars' location and gather the necessary information for corrosion assessment. Although this method has shown good performance in some cases, it exhibits significant limitations. For instance, this method requires predefined thresholds, which may not be universally applicable [131]. In addition, the method is computationally expensive and time-consuming, rendering it unfeasible for large case studies. Furthermore, the method proved to be inefficient when dealing with deteriorated slabs, where the hyperbolic patterns may not be clear enough for accurate recognition using this method [131] [129].

Table 19: Summary of studies devoted to hyperbolic-signature-based rebar localization.

Ref	Test data	Data processing technique	Detection level	Metric	Result
[132]	Field & Synthetic	Cascaded frequency filter + Similarity score	Pixel	F1 score	0.97
[133]	Field	Sub-window resolution + GA	Pixel	Undetected% False detection%	12% 9%
[130]	Field	SSD with adaptive hyperbola model	Pixel	Accuracy	80%-92%
[131]	Field	LSHS migration + thresholding	Pixel	Accuracy	98%-99%
[129]	Field	SSD + partial differential equations.	Pixel	-	-

4.4.2 Rebar recognition using machine learning

Another avenue of research endeavors outlined in

Table 20 focused on utilizing machine learning algorithms to enhance the automated rebar detection process. The general scheme of machine learning (ML) based rebar detection is

outlined in Fig. 26. For instance, Asadi et al. [134] explored the use of an optimized histogram of oriented gradients (HOG) for feature-extraction of hyperbolas in GPR radargrams. The authors studied three boosting classifiers (discrete AdaBoost, real AdaBoost, and gentle Adaboost) for rebar recognition and found that real AdaBoost performed the best. They also implemented an adaptive polynomial filter to remove false detections and improve detection accuracy. In another study, Asadi et al. [135] utilized fine-tuned HOG as a feature descriptor of radargrams. A multi-scale pyramid sliding window was incorporated to identify the region of interest. Multi-layer perceptron (MLP) was trained using four-fold cross-validation on the URIGPR dataset to detect the rebar signature precisely. In addition, Kaur et al. [136] presented a three-stage model for the detection of rebar signatures. In the first stage, the SVM classifier has been trained using HOG of features and utilized to detect the rebar region. Secondly, the region containing the rebar is pruned and refined using statistical analysis to create a bounding box around the hyperbolic signature of the rebar. Finally, the exact rebar location is identified using hyperbolic fitting to identify the hyperbola's peak.

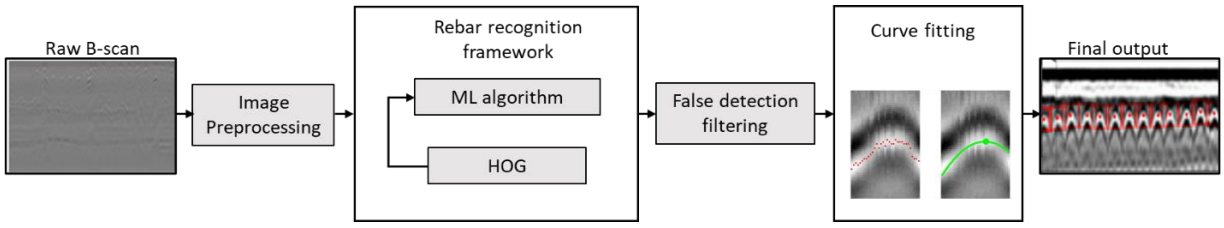

Fig. 26: General scheme of rebar detection using ML algorithms.

Machine Learning (ML) algorithms demonstrate a better overall performance compared to the hyperbolic-signature-based method. The computational expenses and processing time were also reduced. Nonetheless, ML-based detection still exhibits some limitations. For instance, the features of the training data set may differ with the change of GPR device and their collection setups, such as scan/m, samples/scan, and time range. Moreover, the search window may not be universally applicable to all cases, and the overlapping of hyperbolic shapes and

the presence of highly attenuated hyperbolas constitute significant challenges for this method [134,135].

Table 20: Summary of studies devoted to ML-based rebar localization.

Reference	Test data	Data processing technique	Detection type	Metric	Result
[134]	Field	HOG feature extraction + AdaBoost	Bounding box level	-	-
[135]	Field	Fine-tuned HOG + MLP	Bounding box level	Accuracy	81%-93%
[136]	Field	HOG + SVM	Bounding box level	Accuracy	91%-92%

4.4.3 Rebar recognition using deep learning algorithms

The third branch of previous research endeavors used deep learning (DL) algorithms to realize automated recognition of steel rebars. These methods operated either at the pixel level, where each pixel is labeled separately, or within a bounding box context, where the hyperbolic signature is labeled inside a box. At the pixel level, Dinh et al. [137] leveraged the pre-processing procedures of time correction and hyperbolic summation (HS) migration algorithm to prepare the data for rebar picking. The positive peaks in the migrated B-scan are then localized using normalized cross-correlation (NCC) with a global thresholding of 0.45 to indicate a possible rebar location. Afterward, thresholds for expected rebar depth and spacing, along with a deep convolutional neural network (DCNN) consisting of fourteen layers, were employed to filter out the false rebar recognitions. Most recently, Ahmed et al. [138] proposed a novel multistage deep encoder-decoder network to identify rebar in concrete decks, as depicted in Fig. 27. The model was applied at the pixel level, where pixels corresponding to rebars were labeled as 1, and other pixels were labeled as 0. The authors investigated different architectures for the deep network, and it was inferred that the optimal one encompassed SegNet-MobileNet base architectural framework integrated with ResNet-Xception encoder module. The first stage aimed to identify the boundaries of the rebar layers, while the second

stage recognized the rebars' signature. Finally, the outputs of the two stages were crossed to eliminate the rebar signatures outside the rebar layer boundaries.

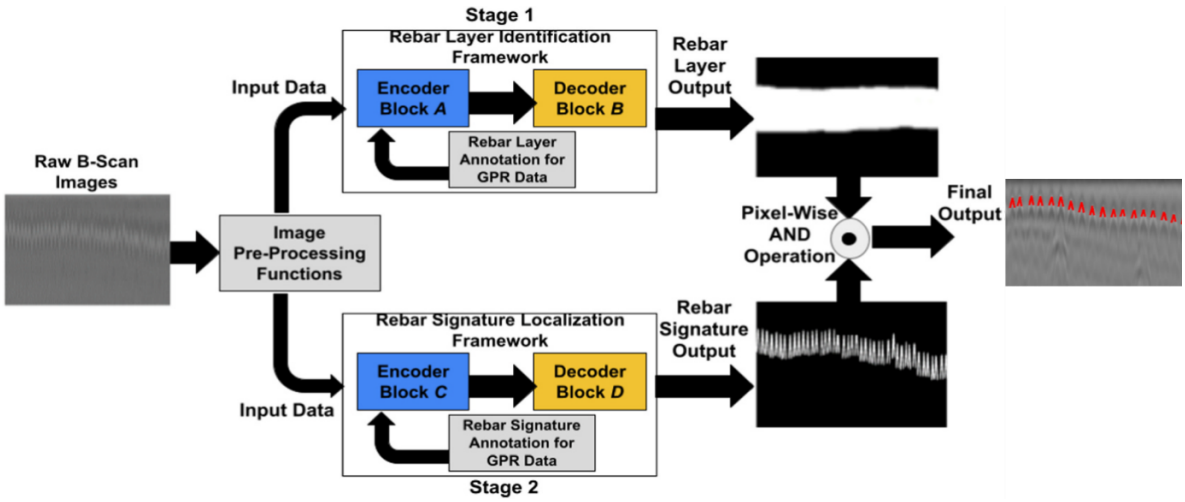

Fig. 27: Multi-Stage Deep Encoder-Decoder Network for Rebar Detection and Localization [138].

In the bounding-box context, Ahmed and Gucunski [139] performed rebar detection based on deep residual networks and K-means clustering, as depicted in Fig. 28 (a). K-means was employed to isolate the rebar regions from the rest of the B-scan data to reduce the search area and enhance detection accuracy. For the rebar detection task, the researchers explored a group of DenseNet and ResNet architectures, which included ResNet-18, ResNet-34, ResNet-50, ResNet-101, ResNet-152, DenseNet-121, and DenseNet-161. It was found that ResNet-152 exhibited better prediction accuracies and training time when compared to the other deep learning architectures. On the same point, Hou et al. [140] presented an approach encompassing mask R-CNN for recognition and segmentation of rebar, as illustrated in Fig. 28 (b). The authors employed distance-guided intersection over union (DGIoU) as a loss training function to diminish the differences between actual and predicted bounding boxes. Finally, thresholding and point extraction, followed by curve fitting, were used to detect the exact location of the rebar signature.

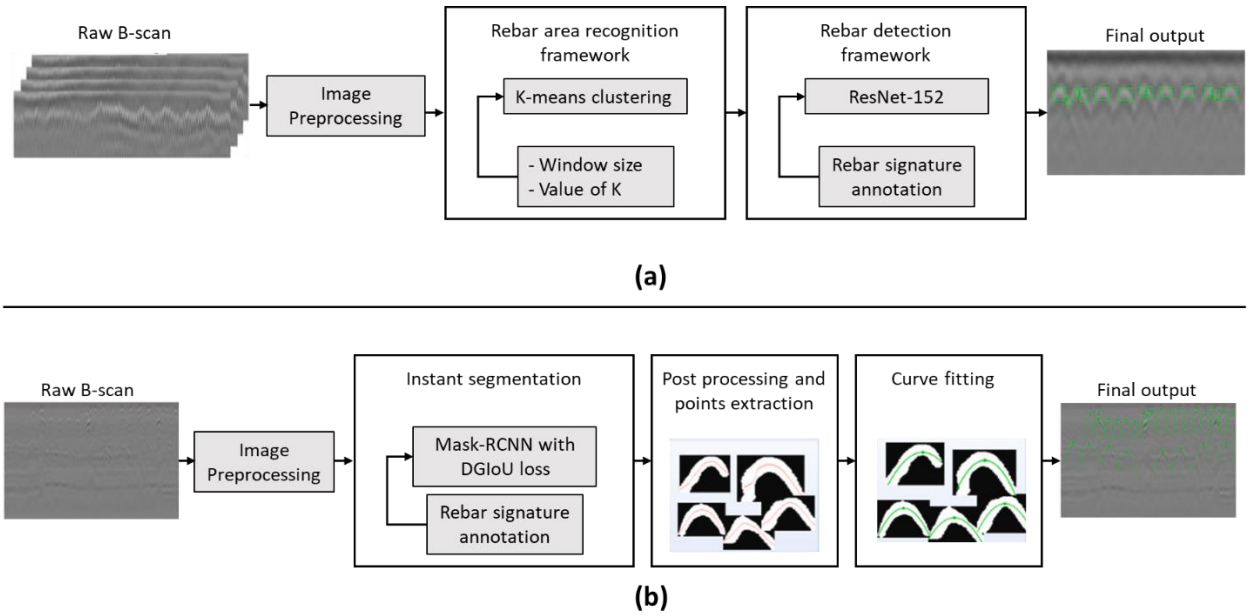

Fig. 28: (a) Rebar detection model based on Kmeans and ResNet-152 [139]. (b) Rebar detection model based on RCNN, DGIoU, and curve fitting [140].

Furthermore, Lei et al. [141] blended convolutional neural networks (CNN) and long short-term memory (LSTM) networks to retrieve hyperbola regions from GPR B-scans. The authors employed the GPR-max toolbox to produce GPR profiles with different situps and applied adaptive normalization to standardize the B-scans before further processing. Finally, the model was validated using real laboratory data. Similarly, as outlined in Fig. 29, Zheng et al. [142] developed a single-shot multi-box detector (SSD) model for rebar localization in a corrosive environment. In the proposed model, truncated VGG-16 (Visual Geometry Group) was used as the base network, and convolutional feature layers were appended to the end of the VGG-16 network. Migration and thresholding were then utilized to localize the hyperbolas apexes.

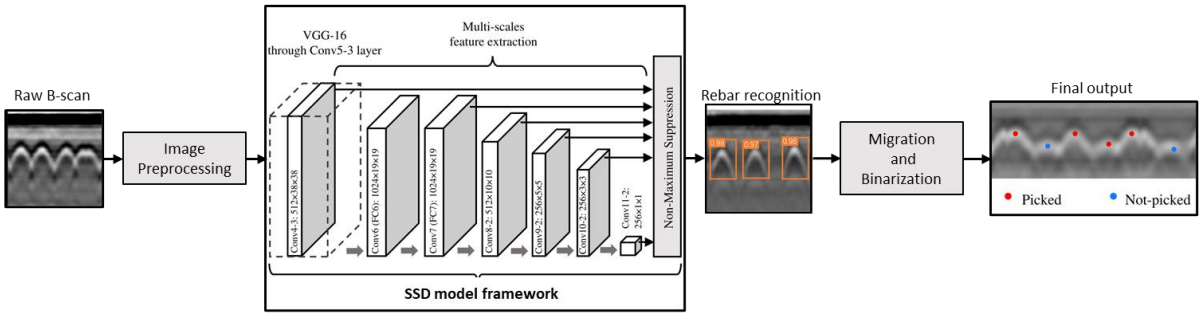

Fig. 29: Rebar detection using SSD model integrated with migration and thresholding postprocessing [142].

Using the methodology shown in Fig. 30, Xiong & Tan [143] compared the performances of YOLO-V4-tiny, YOLO-V3, YOLO-V3-tiny, and YOLO-V4 in the detection of tie bars in concrete pavement. The results indicate that YOLO-V4 provides better-accomplishing precision, recall, F1-score, and mean average precision (map@0.5) of 99.2%, 99.6%, 99.4%, and 99.74%, respectively. Similarly, Yue et al. [144] introduced an improved least square generative adversarial networks (LSGAN) model to augment GPR images. The topology of typical LSGAN was adapted using eight transposed convolutional blocks for the up-sampling of input GPR radargrams. Subsequently, YOLO-V4 was trained using Adam optimizer for detecting rebar in the GPR images. In another study, Park et al. [145] applied frequency–wavenumber migration to consolidate the reflected waves of rebar. YOLO-V3 network was afterward employed for the detection of rebar patterns and the estimation of their diameter.

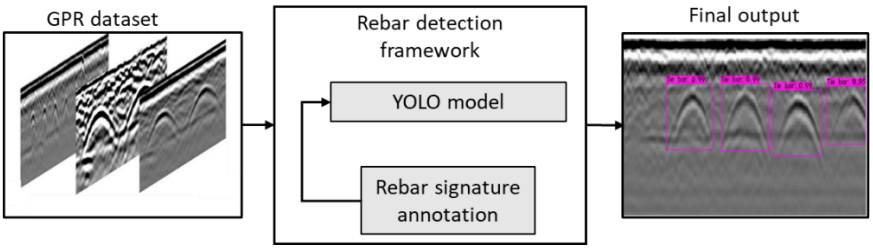

Fig. 30: YOLO framework for rebar detection.

Deep Learning algorithms demonstrate a better overall performance compared to the previous method. Nonetheless, as outlined in Table 21, Deep-learning-based detection still exhibits some limitations. For instance, these algorithms demand substantial amounts of labeled data,

which is time-consuming and may not encompass all potential scenarios. Furthermore, highly attenuated hyperbolas carry significant challenges for this method.

Table 21: Summary of studies devoted to DL-based rebar localization.

Ref	Processing technique	Detection Level	Test type	Metric	Result	Limitations
[138]	Multi-stage deep encoder-decoder network	Pixel	Field	Accuracy	91%	Factors such as high noise, weak signal in deteriorated areas, hyperbolas overlaps, and background reflection affect the picking accuracy.
[143]	YOLO-V4-tiny, YOLO-V4, YOLO-V3-tiny and YOLO-V3	Bounding box	Field	Precision	99%	Training data was insufficient; the model should be tested on deteriorated slaps.
[119]	SSD model	Bounding box	Field	Accuracy	98.0%	The model cannot detect blurred hyperbolas in deteriorated slabs. Requires more training datasets.
[140]	Mask R-CNN + DGIoU	Bounding box	Field	Accuracy	58%	It requires a large amount of data, and the prediction accuracy is relatively low.
[144]	Improved LSGAN + YOLO-V4	Bounding box	Field + Simulated data	Precision	95%	It requires to be trained on more real data to include additional features. The model also should be tested on a deteriorated slab.
[141]	CNN-LSTM + SSMD model	Bounding box	gprMax + Laboratory.	Accuracy	92%	Training data was insufficient, and the model does not function on hyperbolas overlaps.
[146]	Deep residual network + KMC	Bounding box	Field	Precision	91%-97%	The system needs to reduce the false positive rate of the rebar layer identification.
[137]	HS migration + NCC+ DCNN	Pixel	Field	Accuracy	95%-99%	Requires inputs about rebar depth and spacing. Changing the collection setup requires resampling the GPR images.

4.5 GPR-based deterioration modeling

Deterioration modeling plays a crucial role in understanding and managing the condition of concrete structures. The development of deterioration models requires establishing a historical database for the structures [55]. In this context, GPR is relatively recent and not as widely

adopted as other inspection methods, such as imaging and visual inspection. Consequently, GPR-based deterioration modeling is not as prevalent as visual-based deterioration modeling.

More recently, with the emergence of different NDTs, the non-destructive evaluation-based deterioration models became more common, as outlined in Table 22. These models either leveraged GPR corrosion assessment solely as a performance condition indicator or integrated GPR with visual inspection and other NDT for condition assessment. For instance, multiple studies [102,120,147] employed GPR to establish a corrosion condition database for concrete to enable the projection of corrosion levels in concrete bridge decks. The authors employed Weibull distribution functions to develop their models. Similarly, Alsharqawi et al. [148] used Weibull distribution to model ideal and updated deterioration curves of bridge decks based on GPR and visual inspections. In another study, Ghodoosi et al. [37] used GPR to estimate the corrosion level in the upper layer of the concrete deck and utilized non-linear finite element modeling to evaluate the effect of corrosion progression on structure reliability.

A second group of NDT-based deterioration models integrated GPR with other NDTs to realize more comprehensive deterioration modeling. For instance, Kim et al. [149] consolidated the condition indices of GPR, HCP, ER, and IE and deployed sigmoidal regression functions to project the future condition of bridge decks.

Table 22: GPR-based deterioration prediction of concrete bridges.

Reference	**Year**	**Data acquisition method**	**Deterioration modeling method**
[102]	2021	GPR	Weibull distribution
[120]	2020	GPR	Weibull distribution
[149]	2019	GPR+ HCP +IE +ER	Sigmoidal regression function
[148]	2018	GPR + Visual inspection	Weibull distribution
[147]	2018	GPR	Weibull distribution
[37]	2018	GPR and finite element modeling	Non-linear finite element modeling + Best-fit distribution analysis

5 CONCLUSIONS AND FUTURE RESEARCH

In conclusion, this paper emphasizes the critical role of GPR in the assessment of reinforced concrete structures, including bridge decks. Although GPR proved to be effective for data collection and overall assessment, the analysis and interpretation of GPR data are complicated and time-consuming due to various factors affecting GPR waves. This research employed scientometric and systematic reviews to comprehensively understand the GPR data interpretation methods and the impact of physical, environmental, and technical factors on GPR interpretation outcomes. In addition, this study sheds light on potential future directions to improve the efficiency of GPR interpretation for assessing reinforcement in concrete decks.

Based on the literature review on the factors affecting electromagnetic waves, it was found that corrosion by-products increase the amplitude of the reflected wave due to rust propagation into concrete cracks, which increases the reflectivity of the concrete-steel interface. In addition, moisture mainly increases the TWTT and causes limited attenuation to the amplitude of RW and DW. However, when chloride is present alongside moisture, it causes severe attenuation to the DW and RW. Chloride contamination also attenuates the center frequency of DW and RW regardless of moisture presence. Thus, when conducting a numerical analysis, it is recommended to analyze all A-scan components concurrently, including the amplitudes of both reflected and direct waves, as well as the central frequencies and TWTT. The TWTT parameter, alongside wave velocity estimation, can provide essential information about the cover depth and the moisture distribution in the concrete. Similarly, analyzing the frequencies of both reflected and direct waves can help to estimate the level of chloride contamination in the concrete cover. Furthermore, evaluating the attenuation of both reflected and direct waves can provide insight into the presence of corrosion, considering both the moisture and chloride estimates. To this end, Machine Learning (ML) techniques can be an effective tool for performing a comprehensive analysis of A-scan components.

Rebar recognition and information extraction are substantial processes in GPR data analysis. Nonetheless, this process demands considerable labor and time investment. Automated rebar detection in GPR images is complex due to various factors, such as low contrast, low signal-to-noise ratio, and complex field data. The reviewed models lack efficiency in detecting rebars in corrosive environments, particularly when dealing with blurred hyperbolas. Indeed, recognizing blurred hyperbolas is crucial for condition assessment as the blurriness degree represents the corrosiveness of the concrete cover. Therefore, developing methods capable of detecting rebars in corrosive environments is crucial.

The reviewed literature has emphasized the significance of depth correction and amplitude mapping in the numerical analysis of GPR data. However, the absence of a standardized methodology for these processes can result in varying interpretation results. To address this issue, it is recommended to use the actual depth of the concrete cover to calculate the attenuation rate instead of relying solely on attenuation magnitude. This approach could lead to the establishment of standardized thresholds for corrosion assessment, resulting in improved accuracy and reliability of GPR data interpretation. Therefore, it is highly recommended to develop effective methodologies for rebar depth estimation based on experimental work. Moreover, standardized thresholding for the amplitude mapping is recommended by utilizing attenuation rate dB/cm and employing statistical correlation with validation methods for threshold estimation.

Visual analysis of B-scans is considered a more thorough approach than numerical analysis of A-scans due to the uncertainty caused by the complexity of the affecting factors. However, visual analysis can be subjective because it heavily relies on the analyst's judgment, which can lead to variations in the interpretation results. To overcome this challenge, Artificial Intelligence (AI) and computer vision technologies can be employed to automate the analysis of B-scans by identifying key image features such as blurriness, hyperbolic shapes,

reinforcement layer deformation, and slab boundary disappearance. Recent studies have demonstrated the efficacy of machine learning models in automatically detecting rebars in concrete structures, indicating a promising starting point for automating the assessment of B-scan images. Nevertheless, developing more advanced models is essential to comprehensively interpret B-scan images and enhance the accuracy of corrosion assessment.

Augmented reality (AR) technology has the potential to revolutionize the visualization of bridge deck conditions by providing a human-computer interface for real-time 3D visualization of GPR results. By using AR to present GPR data in a 3D format, it would be possible to view the deck condition in a more intuitive and interactive way, which could enhance the ability of inspectors to identify areas of concern. To achieve this, a hybrid system that integrates geographical information systems (GIS), GPR, and artificial intelligence (AI) would be required. The GIS component would provide the spatial information necessary to locate the bridge deck, while GPR would provide the subsurface data. AI algorithms could process the GPR data in real-time and generate visualizations overlaid onto the bridge deck via the AR interface.

Author Contributions, Nour Faris: Conceptualization, methodology, formal analysis, data curation, investigation, resources, original draft preparation writing, and review and editing. Tarek Zayed: Administration, funding, and review and editing. Eslam Mohammed Abdelkader: Conceptualization, methodology, formal analysis, data curation, investigation, resources, writing original draft preparation writing, and review and editing. Ali Fares: Writing original draft preparation writing, review, and editing. All authors have read and agreed to the published version of the manuscript.

Funding: The authors gratefully acknowledge the support from the Smart Traffic Fund (STF) under grant number PSRI/14/2109/RA.

Institutional Review Board Statement: Not applicable.

Informed Consent Statement: Informed consent was obtained from all subjects involved in the study.

Data Availability Statement: Some or all data that support the findings of this study are available from the corresponding author upon reasonable request.

Conflicts of Interest: The authors declare no conflict of interest.

References

[1] G.M. Hadjidemetriou, X. Xie, A.K. Parlikad, Predictive Group Maintenance Model for Networks of Bridges, Transp. Res. Rec. 2674 (2020) 373–383. https://doi.org/10.1177/0361198120912226.

[2] Y. Li, Y. Dong, D.M. Frangopol, D. Gautam, Long-term resilience and loss assessment of highway bridges under multiple natural hazards, Struct. Infrastruct. Eng. 16 (2020) 626–641. https://doi.org/10.1080/15732479.2019.1699936.

[3] E. Fereshtehnejad, G. Gazzola, P. Parekh, C. Nakrani, H. Parvardeh, Detecting Anomalies in National Bridge Inventory Databases Using Machine Learning Methods, Transp. Res. Rec. 2676 (2022) 453–467. https://doi.org/10.1177/03611981221075028.

[4] CIRC, Canada Infrastructure Report Card 2019, Can. Infrustructure. (2019) 1–56. http://canadianinfrastructure.ca/en/about.html.

[5] S. Gohar, Y. Matsumoto, T. Maki, S. Sakuma, Investigation into vibration-based structural damage identification and amplitude-dependent damping ratio of reinforced concrete bridge deck slab under different loading states, J. Civ. Struct. Heal. Monit. 13 (2023) 133–148. https://doi.org/10.1007/s13349-022-00625-w.

[6] E.S. Cavaco, A. Bastos, F. Santos, Effects of corrosion on the behaviour of precast concrete floor systems, Constr. Build. Mater. 145 (2017) 411–418. https://doi.org/10.1016/j.conbuildmat.2017.04.044.

[7] D.H. Yang, G.P. Li, T.H. Yi, H.N. Li, A performance-based service life design method for reinforced concrete structures under chloride environment, Constr. Build. Mater. 124 (2016) 453–461. https://doi.org/10.1016/j.conbuildmat.2016.07.127.

[8] G. Choe, Y. Shinohara, G. Kim, S. Lee, E. Lee, J. Nam, Concrete corrosion cracking and transverse bar strain behavior in a reinforced concrete column under simulated marine conditions, Appl. Sci. 10 (2020). https://doi.org/10.3390/app10051794.

[9] E.M. Abdelkader, T. Zayed, N. Faris, Synthesized Evaluation of Reinforced Concrete Bridge Defects, Their Non-Destructive Inspection and Analysis Methods: A Systematic Review and Bibliometric Analysis of the Past Three Decades, Buildings. 13 (2023). https://doi.org/10.3390/buildings13030800.

[10] J.Y. Rhee, J.J. Choi, S.H. Kee, Evaluation of the Depth of Deteriorations in Concrete Bridge Decks with Asphalt Overlays Using Air-Coupled GPR: A Case Study from a Pilot Bridge on Korean Expressway, Int. J. Concr. Struct. Mater. 13 (2019). https://doi.org/10.1186/s40069-018-0327-7.

[11] S. Wang, Z. Leng, X. Sui, Detectability of concealed cracks in the asphalt pavement layer using air-coupled ground-penetrating radar, Meas. J. Int. Meas. Confed. 208 (2023) 112427. https://doi.org/10.1016/j.measurement.2022.112427.

[12] S. Echchakoui, Why and how to merge Scopus and Web of Science during bibliometric analysis: the case of sales force literature from 1912 to 2019, J. Mark. Anal. 8 (2020) 165–184. https://doi.org/10.1057/s41270-020-00081-9.

[13] Scopus, The Scopus Content Coverage Guide: A complete overview of the content coverage in Scopus and corresponding policies, (2023). http://surl.li/luwon (accessed October 5, 2023).

[14] A. Tarussov, M. Vandry, A. De La Haza, Condition assessment of concrete structures using a new analysis method: Ground-penetrating radar computer-assisted visual interpretation, Constr. Build. Mater. 38 (2013) 1246–1254. https://doi.org/10.1016/j.conbuildmat.2012.05.026.

[15] K. Maser, N. Martino, J. Doughty, R. Birken, Understanding and detecting bridge deck deterioration with ground-penetrating radar, Transp. Res. Rec. (2012) 116–123. https://doi.org/10.3141/2313-13.

[16] ASTM D6087, Standard Test Method for Evaluating Asphalt-Covered Concrete Bridge Decks Using Ground Penetrating Radar, D6087-08 (2008) 1790–1793. https://doi.org/10.1520/D6087-08.

[17] C.L. Barnes, J.F. Trottier, D. Forgeron, Improved concrete bridge deck evaluation using GPR by accounting for signal depth-amplitude effects, NDT E Int. 41 (2008) 427–433. https://doi.org/10.1016/j.ndteint.2008.03.005.

[18] ASTM D6087, Standard test method for evaluating asphalt-covered concrete bridge decks using ground penetrating radar, D6087-08R1 (2010). https://doi.org/10.1520/D6087-08R15E01.

[19] World Bank, World Bank Blogs, (2023). https://blogs.worldbank.org/opendata/new-world-bank-country-classifications-income-level-2022-2023 (accessed September 6, 2023).

[20] C. Rehn, D. Wadskog, C. Gornitzki, A. Larsson, Bibliometric Indicators - Definitions and Usage at Karolinska Institutet, Karolinska Institutet. (2014) 19. http://kib.ki.se/sites/default/files/bildarkiv/Dokument/bibliometric_indicators_2014.pdf.

[21] S. Abdelkhalek, T. Zayed, Performance assessment model of non-destructive technologies in inspecting concrete bridge decks, Struct. Infrastruct. Eng. 19 (2023) 216–237. https://doi.org/10.1080/15732479.2021.1937234.

[22] S. Abdelkhalek, T. Zayed, Performance assessment model of non-destructive technologies in inspecting concrete bridge decks, Struct. Infrastruct. Eng. 0 (2021) 1–22. https://doi.org/10.1080/15732479.2021.1937234.

[23] B.R. Taylor, Y. Qiao, M.D. Bowman, S. Labi, The Economic Impact of Implementing Nondestructive Testing of Reinforced Concrete Bridge Decks in Indiana, 2016. https://doi.org/10.5703/1288284316343.

[24] N. Gucunski, A. Imani, F. Romero, S. Nazarian, D. Yuan, H. Wiggenhauser, P. Shokouhi, A. Taffe, D. Kutrubes, Nondestructive Testing to Identify Concrete Bridge Deck Deterioration, Transportation Research Board, Washington, D.C., 2012. https://doi.org/10.17226/22771.

[25] S. Abdelkhalek, Managing the inspection process of concrete bridge decks, The Hong Kong Polytechnic University, 2022. https://theses.lib.polyu.edu.hk/handle/200/11748.

[26] N. Gucunski, B. Pailes, J. Kim, H. Azari, K. Dinh, Capture and Quantification of Deterioration Progression in Concrete Bridge Decks through Periodical NDE Surveys, J. Infrastruct. Syst. 23 (2017) 1–11. https://doi.org/10.1061/(asce)is.1943-555x.0000321.

[27] T.W. Robison, C.L. Barnes, Y. Tinkey, J.E. Tanner, Evaluating concrete damage in

bridge decks with and without overlays using nondestructive testing procedures, J. Test. Eval. 48 (2020). https://doi.org/10.1520/JTE20180555.

[28] A. Zaki, M.A.M. Johari, W.M.A.W. Hussin, Y. Jusman, Experimental Assessment of Rebar Corrosion in Concrete Slab Using Ground Penetrating Radar (GPR), Int. J. Corros. 2018 (2018). https://doi.org/10.1155/2018/5389829.

[29] İ. Kaplanvural, K. Özkap, E. Pekşen, Influence of water content investigation on GPR wave attenuation for early age concrete in natural air-drying condition, Constr. Build. Mater. 297 (2021). https://doi.org/10.1016/j.conbuildmat.2021.123783.

[30] N.J. Cassidy, Ground Penetrating Radar Data Processing, Modelling and Analysis, First Edit, Elsevier, 2008. https://doi.org/10.1016/B978-0-444-53348-7.00005-3.

[31] K. Belli, S. Wadia-Fascetti, C. Rappaport, Model based evaluation of bridge decks using ground penetrating radar, Comput. Civ. Infrastruct. Eng. 23 (2008) 3–16. https://doi.org/10.1111/j.1467-8667.2007.00516.x.

[32] G. Leucci, Ground Penetrating Radar: an Application to Estimate Volumetric Water Content and Reinforced Bar Diameter in Concrete Structures, J. Adv. Concr. Technol. 10 (2012) 411–422. https://doi.org/10.3151/jact.10.411.

[33] L. Tasker, A. Karrech, J. Shragge, M. Josh, Time-lapse monitoring of internal alteration of a concrete structure using ground penetrating radar, Constr. Build. Mater. 191 (2018) 300–310. https://doi.org/10.1016/j.conbuildmat.2018.10.008.

[34] S. Laurens, J.P. Balayssac, J. Rhazi, G. Arliguie, Influence of concrete relative humidity on the amplitude of ground-penetrating radar (GPR) signal, Mater. Struct. Constr. 34 (2002) 198–203. https://doi.org/10.1617/13815.

[35] S. Hong, H. Wiggenhauser, R. Helmerich, B. Dong, P. Dong, F. Xing, Long-term monitoring of reinforcement corrosion in concrete using ground penetrating radar, Corros. Sci. 114 (2017) 123–132. https://doi.org/10.1016/j.corsci.2016.11.003.

[36] C.W. Chang, C.A. Tsai, Y.C. Shiau, Inspection of Steel Bars Corrosion in Reinforced Concrete Structures by Nondestructive Ground Penetrating Radar, Appl. Sci. 12 (2022). https://doi.org/10.3390/app12115567.

[37] F. Ghodoosi, A. Bagchi, T. Zayed, M.R. Hosseini, Method for developing and updating deterioration models for concrete bridge decks using GPR data, Autom. Constr. 91 (2018) 133–141. https://doi.org/10.1016/j.autcon.2018.03.014.

[38] G.S.S. Inc., Geophysical Survey System Inc., (2023). https://www.geophysical.com/ (accessed August 23, 2023).

[39] I. dei Sistemi, Ingegneria dei Sistemi, (2023). https://idsgeoradar.com/ (accessed August 23, 2023).

[40] J.R.C. Ltd., Japan Radio Co. Ltd., (2023). https://www.jrc.co.jp/en/ (accessed August 23, 2023).

[41] S.& S. Inc., Sensors & Software Inc., (2023). https://www.sensoft.ca/ (accessed August 23, 2023).

[42] S.E. Technologies, Screening Eagle Technologies, (2023). https://www.screeningeagle.com/ (accessed August 23, 2023).

[43] G. Geo., Guideline Geo., (2023). https://www.guidelinegeo.com/ (accessed August 10, 2023).

[44] U.E. Ltd., Utsi Electronics Ltd., (2023). https://pipehawk.uk/ (accessed August 23, 2023).

[45] P. Corporation, Penetradar Corporation, (2023). http://penetradar.com/new/ (accessed August 23, 2023).

[46] I. Radar Systems, Radar Systems, Inc., (2023). http://www.radsys.lv/en/index/ (accessed August 23, 2023).

[47] ImpulseRadar, ImpulseRadar, (2023). https://impulseradargpr.com/ (accessed August 10, 2023).

[48] A.M. Plattner, GPRPy: Open-source ground-penetrating radar processing and visualization software, Lead. Edge. 39 (2020) 332–337. https://doi.org/10.1190/tle39050332.1.

[49] K.-J. Sandmeier, Reflexw, (2023). https://www.sandmeier-geo.de/reflexw.html (accessed August 23, 2023).

[50] GPRSoft, GPRSoft, (2020). https://groundsearch.biz/product/software/ (accessed August 21, 2023).

[51] Geolitix, Geolitix, (2023). https://www.geolitix.com/ (accessed August 23, 2023).

[52] GPRmax, GPRmax, (2023). https://www.gprmax.com/ (accessed August 23, 2023).

[53] H. Liu, J. Zhong, F. Ding, X. Meng, C. Liu, J. Cui, Detection of early-stage rebar corrosion using a polarimetric ground penetrating radar system, Constr. Build. Mater. 317 (2022) 125768. https://doi.org/10.1016/j.conbuildmat.2021.125768.

[54] Z. Xiang, A. Rashidi, G. Ou, Automated Framework to Translate Rebar Spatial Information from GPR into BIM, J. Constr. Eng. Manag. 147 (2021) 1–13. https://doi.org/10.1061/(asce)co.1943-7862.0002141.

[55] T. Dawood, Z. Zhu, T. Zayed, Deterioration mapping in subway infrastructure using sensory data of GPR, Tunn. Undergr. Sp. Technol. 103 (2020) 103487. https://doi.org/10.1016/j.tust.2020.103487.

[56] J.Y. Rhee, S.H. Kee, H.S. Kim, J.J. Choi, Seasonal Variation and Age-related Changes in the Relative Permittivity of Concrete Bridge Decks on Korea Expressways, Int. J. Concr. Struct. Mater. 12 (2018). https://doi.org/10.1186/s40069-018-0239-6.

[57] T. Omar, M.L. Nehdi, T. Zayed, Rational Condition Assessment of RC Bridge Decks Subjected to Corrosion-Induced Delamination, J. Mater. Civ. Eng. 30 (2018) 1–13. https://doi.org/10.1061/(asce)mt.1943-5533.0002114.

[58] R. Du Plooy, S. Palma Lopes, G. Villain, X. Dérobert, Development of a multi-ring resistivity cell and multi-electrode resistivity probe for investigation of cover concrete condition, NDT E Int. 54 (2013) 27–36. https://doi.org/10.1016/j.ndteint.2012.11.007.

[59] H.M. La, N. Gucunski, S.H. Kee, L. Van Nguyen, Data analysis and visualization for the bridge deck inspection and evaluation robotic system, Vis. Eng. 3 (2015). https://doi.org/10.1186/s40327-015-0017-3.

[60] S.J. Radzevicius, J.J. Daniels, Ground penetrating radar polarization and scattering from cylinders, J. Appl. Geophys. 45 (2000) 111–125. https://doi.org/10.1016/S0926-9851(00)00023-9.

[61] L. Zanzi, D. Arosio, Sensitivity and accuracy in rebar diameter measurements from dual-polarized GPR data, Constr. Build. Mater. 48 (2013) 1293–1301. https://doi.org/10.1016/j.conbuildmat.2013.05.009.

[62] K. Dinh, N. Gucunski, K. Tran, A. Novo, T. Nguyen, Full-resolution 3D imaging for concrete structures with dual-polarization GPR, Autom. Constr. 125 (2021) 103652. https://doi.org/10.1016/j.autcon.2021.103652.

[63] H. Liu, H. Lu, J. Lin, F. Han, C. Liu, J. Cui, B.F. Spencer, Penetration Properties of Ground Penetrating Radar Waves through Rebar Grids, IEEE Geosci. Remote Sens. Lett. 18 (2021) 1199–1203. https://doi.org/10.1109/LGRS.2020.2995670.

[64] J. Hugenschmidt, A. Kalogeropoulos, F. Soldovieri, G. Prisco, Processing strategies for high-resolution GPR concrete inspections, NDT E Int. 43 (2010) 334–342. https://doi.org/10.1016/j.ndteint.2010.02.002.

[65] M.R. Shaw, T.C.K. Molyneaux, S.G. Millard, M.J. Taylor, J.H. Bungey, Assessing bar size of steel reinforcement in concrete using ground penetrating radar and neural networks, Insight Non-Destructive Test. Cond. Monit. 45 (2003) 813–816. https://doi.org/10.1784/insi.45.12.813.52980.

[66] X. Ferrieres, G. Klysz, V. Guihard, M. Albrand, Study of the dielectric gradient values of reinforced concrete sample by considering radar measurements in an inverse problem, Inverse Probl. Sci. Eng. 29 (2021) 2–16. https://doi.org/10.1080/17415977.2020.1763339.

[67] K. Agred, G. Klysz, J.P. Balayssac, Location of reinforcement and moisture assessment in reinforced concrete with a double receiver GPR antenna, Constr. Build. Mater. 188 (2018) 1119–1127. https://doi.org/10.1016/j.conbuildmat.2018.08.190.

[68] M.I. Hasan, N. Yazdani, An experimental study for quantitative estimation of rebar corrosion in concrete using ground penetrating radar, J. Eng. (United Kingdom). 2016 (2016). https://doi.org/10.1155/2016/8536850.

[69] F. Zhou, Z. Chen, H. Liu, J. Cui, B.F. Spencer, G. Fang, Simultaneous estimation of rebar diameter and cover thickness by a GPR-EMI dual sensor, Sensors (Switzerland). 18 (2018) 1–15. https://doi.org/10.3390/s18092969.

[70] R. Sahamitmongkol, Effect of scanning direction on amplitude of reflected pulse radar from steel bar, J. Build. Apprais. 6 (2010) 21–33. https://doi.org/10.1057/jba.2010.11.

[71] S.F. Senin, R. Hamid, J. Ahmad, M.I.F. Rosli, A. Yusuff, R. Rohim, K.D. Abdul Ghani, S. Mohamed Noor, Damage detection of artificial corroded rebars and quantification using non-destructive methods on reinforced concrete structure, J. Phys. Conf. Ser. 1349 (2019). https://doi.org/10.1088/1742-6596/1349/1/012044.

[72] V. Sossa, V. Pérez-Gracia, R. González-Drigo, M.A. Rasol, Lab non destructive test to analyze the effect of corrosion on ground penetrating radar scans, Remote Sens. 11 (2019). https://doi.org/10.3390/rs11232814.

[73] J. Lachowicz, M. Rucka, 3-D finite-difference time-domain modelling of ground penetrating radar for identification of rebars in complex reinforced concrete structures,

Arch. Civ. Mech. Eng. 18 (2018) 1228–1240. https://doi.org/10.1016/j.acme.2018.01.010.

[74] M.I. Hasan, N. Yazdani, An Experimental and Numerical Study on Embedded Rebar Diameter in Concrete Using Ground Penetrating Radar, Chinese J. Eng. 2016 (2016). https://doi.org/10.1155/2016/9714381.

[75] K. Dinh, N. Gucunski, J. Kim, T.H. Duong, Understanding depth-amplitude effects in assessment of GPR data from concrete bridge decks, NDT E Int. 83 (2016) 48–58. https://doi.org/10.1016/j.ndteint.2016.06.004.

[76] J.Y. Rhee, J. Shim, S.H. Kee, S.Y. Lee, Different Characteristics of Radar Signal Attenuation Depending on Concrete Condition of Bare Bridge Deck, KSCE J. Civ. Eng. 24 (2020) 2049–2062. https://doi.org/10.1007/s12205-020-1840-1.

[77] C.L. Barnes, J.F. Trottier, Phenomena and conditions in bridge decks that confound ground-penetrating radar data analysis, Transp. Res. Rec. (2002) 57–61. https://doi.org/10.3141/1795-07.

[78] S. Hong, D. Chen, B. Dong, Numerical simulation and mechanism analysis of GPR-based reinforcement corrosion detection, Constr. Build. Mater. 317 (2022) 125913. https://doi.org/10.1016/j.conbuildmat.2021.125913.

[79] K. Tesic, A. Baricevic, M. Serdar, N. Gucunski, Characterization of ground penetrating radar signal during simulated corrosion of concrete reinforcement, Autom. Constr. 143 (2022) 104548. https://doi.org/10.1016/j.autcon.2022.104548.

[80] D. Meng, S. Lin, H. Azari, Nondestructive corrosion evaluation of reinforced concrete bridge decks with overlays: An experimental study, J. Test. Eval. 48 (2020) 516–537. https://doi.org/10.1520/JTE20180388.

[81] M.N. Soutsos, J.H. Bungey, S.G. Millard, M.R. Shaw, A. Patterson, Dielectric properties of concrete and their influence on radar testing, NDT E Int. 34 (2001) 419–425. https://doi.org/10.1016/S0963-8695(01)00009-3.

[82] Z.M. Sbartaï, S. Laurens, J.P. Balayssac, G. Arliguie, G. Ballivy, Ability of the direct wave of radar ground-coupled antenna for NDT of concrete structures, NDT E Int. 39 (2006) 400–407. https://doi.org/10.1016/j.ndteint.2005.11.003.

[83] G. Klysz, J.P. Balayssac, Determination of volumetric water content of concrete using ground-penetrating radar, Cem. Concr. Res. 37 (2007) 1164–1171. https://doi.org/10.1016/j.cemconres.2007.04.010.

[84] K. Viriyametanont, S. Laurens, G. Klysz, J.P. Balayssac, G. Arliguie, Radar survey of concrete elements: Effect of concrete properties on propagation velocity and time zero, NDT E Int. 41 (2008) 198–207. https://doi.org/10.1016/j.ndteint.2007.10.001.

[85] S.F. Senin, R. Hamid, Ground penetrating radar wave attenuation models for estimation of moisture and chloride content in concrete slab, Constr. Build. Mater. 106 (2016) 659–669. https://doi.org/10.1016/j.conbuildmat.2015.12.156.

[86] J. Lachowicz, M. Rucka, A novel heterogeneous model of concrete for numerical modelling of ground penetrating radar, Constr. Build. Mater. 227 (2019) 116703. https://doi.org/10.1016/j.conbuildmat.2019.116703.

[87] Y. Li, H. Zhang, S. Chen, H. Wang, G. Liu, Multi-scale study on the durability

degradation mechanism of aeolian sand concrete under freeze–thaw conditions, Constr. Build. Mater. 340 (2022) 127433. https://doi.org/10.1016/j.conbuildmat.2022.127433.

[88] A. Peyman, C. Gabriel, E.H. Grant, Complex permittivity of sodium chloride solutions at microwave frequencies, Bioelectromagnetics. 28 (2007) 264–274. https://doi.org/10.1002/bem.20271.

[89] R. du Plooy, G. Villain, S. Palma Lopes, A. Ihamouten, X. Dérobert, B. Thauvin, Electromagnetic non-destructive evaluation techniques for the monitoring of water and chloride ingress into concrete: a comparative study, Mater. Struct. Constr. 48 (2015) 369–386. https://doi.org/10.1617/s11527-013-0189-z.

[90] A. Kalogeropoulos, J. Van Der Kruk, J. Hugenschmidt, J. Bikowski, E. Brühwiler, Full-waveform GPR inversion to assess chloride gradients in concrete, NDT E Int. 57 (2013) 74–84. https://doi.org/10.1016/j.ndteint.2013.03.003.

[91] P.T. wai Wong, W.W. lok Lai, Characterization of Complex Dielectric Permittivity of Concrete by GPR Numerical Simulation and Spectral Analysis, J. Nondestruct. Eval. 41 (2022) 1–15. https://doi.org/10.1007/s10921-021-00836-z.

[92] S. Hong, W.W.L. Lai, G. Wilsch, R. Helmerich, R. Helmerich, T. Günther, H. Wiggenhauser, Periodic mapping of reinforcement corrosion in intrusive chloride contaminated concrete with GPR, Constr. Build. Mater. 66 (2014) 671–684. https://doi.org/10.1016/j.conbuildmat.2014.06.019.

[93] W.L. Lai, T. Kind, H. Wiggenhauser, Using ground penetrating radar and timefrequency analysis to characterize construction materials, NDT E Int. 44 (2011) 111–120. https://doi.org/10.1016/j.ndteint.2010.10.002.

[94] S. Hong, W.L. Lai, R. Helmerich, Experimental monitoring of chloride-induced reinforcement corrosion and chloride contamination in concrete with ground-penetrating radar, Struct. Infrastruct. Eng. 11 (2015) 15–26. https://doi.org/10.1080/15732479.2013.879321.

[95] W.-L. Lai, T. Kind, M. Stoppel, H. Wiggenhauser, Measurement of Accelerated Steel Corrosion in Concrete Using Ground-Penetrating Radar and a Modified Half-Cell Potential Method, J. Infrastruct. Syst. 19 (2013) 205–220. https://doi.org/10.1061/(asce)is.1943-555x.0000083.

[96] P.T.W. Wong, W.W.L. Lai, J.F.C. Sham, C. sun Poon, Hybrid non-destructive evaluation methods for characterizing chloride-induced corrosion in concrete, NDT E Int. 107 (2019) 102123. https://doi.org/10.1016/j.ndteint.2019.05.008.

[97] T.T. Nguyen, P.T. Tung, N.N. Tan, N.N. Linh, T.T. Luc, A Study of Factors Affecting GPR Signal Amplitudes in Reinforced Structures Using Deep Belief Networks, Infrastructures. 7 (2022). https://doi.org/10.3390/infrastructures7090123.

[98] W. Zatar, T.T. Nguyen, H. Nguyen, Predicting GPR Signals from Concrete Structures Using Artificial Intelligence-Based Method, Adv. Civ. Eng. 2021 (2021). https://doi.org/10.1155/2021/6610805.

[99] M. Abouhamad, T. Dawood, A. Jabri, M. Alsharqawi, T. Zayed, Corrosiveness mapping of bridge decks using image-based analysis of GPR data, Autom. Constr. 80 (2017) 104–117. https://doi.org/10.1016/j.autcon.2017.03.004.

[100] N. Gucunski, A. Maher, H. Ghasemi, Condition assessment of concrete bridge decks

using a fully autonomous robotic NDE platform, Bridg. Struct. 9 (2013) 123–130. https://doi.org/10.3233/BRS-130058.

[101] A. Benedetto, G. Manacorda, A. Simi, F. Tosti, Novel perspectives in bridges inspection using GPR, Nondestruct. Test. Eval. 27 (2012) 239–251. https://doi.org/10.1080/10589759.2012.694883.

[102] M. Ata, M. Abouhamad, M. Hassanien Serror, M. Marzouk, Data Acquisition and Structural Analysis for Bridge Deck Condition Assessment Using Ground Penetration Radar, J. Perform. Constr. Facil. 35 (2021) 1–15. https://doi.org/10.1061/(asce)cf.1943-5509.0001645.

[103] A. V. Varnavina, A.K. Khamzin, L.H. Sneed, E. V. Torgashov, N.L. Anderson, N.H. Maerz, K.J. Boyko, Concrete bridge deck assessment: Relationship between GPR data and concrete removal depth measurements collected after hydrodemolition, Constr. Build. Mater. 99 (2015) 26–38. https://doi.org/10.1016/j.conbuildmat.2015.09.008.

[104] K. Dinh, T. Zayed, S. Moufti, A. Shami, A. Jabri, M. Abouhamad, T. Dawood, Clustering-based threshold model for condition assessment of concrete bridge decks with ground-penetrating radar, Transp. Res. Rec. 2522 (2015) 81–89. https://doi.org/10.3141/2522-08.

[105] K. Dinh, T. Zayed, F. Romero, A. Tarussov, Method for Analyzing Time-Series GPR Data of Concrete Bridge Decks, J. Bridg. Eng. 20 (2015) 04014086. https://doi.org/10.1061/(asce)be.1943-5592.0000679.

[106] D. Eisenmann, F. Margetan, C.P.T. Chiou, R. Roberts, S. Wendt, Ground penetrating radar applied to rebar corrosion inspection, AIP Conf. Proc. 1511 (2013) 1341–1348. https://doi.org/10.1063/1.4789198.

[107] H. Sun, S. Pashoutani, J. Zhu, Nondestructive evaluation of concrete bridge decks with automated acoustic scanning system and ground penetrating radar, Sensors (Switzerland). 18 (2018). https://doi.org/10.3390/s18061955.

[108] S. Pashoutani, J. Zhu, Ground Penetrating Radar Data Processing for Concrete Bridge Deck Evaluation, J. Bridg. Eng. 25 (2020) 1–11. https://doi.org/10.1061/(asce)be.1943-5592.0001566.

[109] N. Martino, K. Maser, R. Birken, M. Wang, Quantifying Bridge Deck Corrosion Using Ground Penetrating Radar, Res. Nondestruct. Eval. 27 (2016) 112–124. https://doi.org/10.1080/09349847.2015.1067342.

[110] S. Pashoutani, J. Zhu, Real Depth-Correction in Ground Penetrating RADAR Data Analysis for Bridge Deck Evaluation, Sensors. 23 (2023) 1027. https://doi.org/10.3390/s23021027.

[111] F.A. Romero, C.L. Barnes, H. Azari, S. Nazarian, C.D. Rascoe, Validation of Benefits of Automated Depth Correction Method Improving Accuracy of Ground-Penetrating Radar Deck Deterioration Maps, Transp. Res. Rec. 2522 (2015) 100–109. https://doi.org/10.3141/2522-10.

[112] Geophysical Survey Systems Inc., RADAN 7 manual, 2017. https://www.geophysical.com/wp-content/uploads/2017/10/GSSI-RADAN-7-Manual.pdf.

[113] M. Hashim, S.W. Jaw, M. Marghany, Ground penetrating radar data processing for

retrieval of utility material types and radius estimation, 2011 IEEE Int. RF Microw. Conf. RFM 2011 - Proc. (2011) 191–196. https://doi.org/10.1109/RFM.2011.6168727.

[114] ASTM D6087, Test method for evaluating asphalt-covered concrete bridge decks using ground penetrating radar, Prog. Electromagn. Res. Symp. D6087-11 (2011). https://doi.org/10.1520/D6087-22.

[115] C. Özdemir, Ş. Demirci, E. Yiğit, B. Yilmaz, A review on migration methods in b-scan ground penetrating radar imaging, Math. Probl. Eng. 2014 (2014). https://doi.org/10.1155/2014/280738.

[116] X. Wei, Y. Zhang, Autofocusing techniques for GPR data from RC bridge decks, IEEE J. Sel. Top. Appl. Earth Obs. Remote Sens. 7 (2014) 4860–4868. https://doi.org/10.1109/JSTARS.2014.2321710.

[117] Z. Xiang, G. Ou, A. Rashidi, Integrated Approach to Simultaneously Determine 3D Location and Size of Rebar in GPR Data, J. Perform. Constr. Facil. 34 (2020) 1–12. https://doi.org/10.1061/(asce)cf.1943-5509.0001502.

[118] P. Wiwatrojanagul, R. Sahamitmongkol, S. Tangtermsirikul, N. Khamsemanan, A new method to determine locations of rebars and estimate cover thickness of RC structures using GPR data, Constr. Build. Mater. 140 (2017) 257–273. https://doi.org/10.1016/j.conbuildmat.2017.02.126.

[119] Y.-C. Zhang, T.-H. Yi, S. Lin, H.-N. Li, S. Lv, Automatic Corrosive Environment Detection of RC Bridge Decks from Ground-Penetrating Radar Data Based on Deep Learning, J. Perform. Constr. Facil. 36 (2022) 1–9. https://doi.org/10.1061/(asce)cf.1943-5509.0001712.

[120] M. Alsharqawi, T. Zayed, A. Shami, Ground penetrating radar-based deterioration assessment of RC bridge decks, Constr. Innov. 20 (2020) 1–17. https://doi.org/10.1108/CI-08-2019-0076.

[121] E. Mohammed Abdelkader, M. Marzouk, T. Zayed, An optimization-based methodology for the definition of amplitude thresholds of the ground penetrating radar, Soft Comput. 23 (2019) 12063–12086. https://doi.org/10.1007/s00500-019-03764-3.

[122] J. Feng, L. Yang, E. Hoxha, J. Xiao, Improving 3D Metric GPR Imaging Using Automated Data Collection and Learning-based Processing, IEEE Sens. J. XX (2022) 1–13. https://doi.org/10.1109/JSEN.2022.3164707.

[123] G. Kilic, A. Caner, Augmented reality for bridge condition assessment using advanced non-destructive techniques, Struct. Infrastruct. Eng. 17 (2021) 977–989. https://doi.org/10.1080/15732479.2020.1782947.

[124] K. Dinh, T. Zayed, GPR-Based Fuzzy Model for Bridge Deck Corrosiveness Index, J. Perform. Constr. Facil. 30 (2016) 04015069. https://doi.org/10.1061/(asce)cf.1943-5509.0000815.

[125] C.L. Barnes, J.-F. Trottier, Ground-Penetrating Radar for Network-Level Concrete Deck Repair Management, J. Transp. Eng. 126 (2000) 257–262. https://doi.org/10.1061/(ASCE)0733-947X(2000)126:3(257).

[126] E. Ichi, F. Jafari, S. Dorafshan, SDNET2021: Annotated NDE Dataset for Subsurface Structural Defects Detection in Concrete Bridge Decks, Infrastructures. 7 (2022). https://doi.org/10.3390/infrastructures7090107.

[127] G. Kilic, M.S. Unluturk, Wavelet analysis with different frequency GPR antennas for bridge health assessment, J. Test. Eval. 44 (2016) 647–655. https://doi.org/10.1520/JTE20140321.

[128] D.G. Goulias, S. Cafiso, A. Di Graziano, S.G. Saremi, V. Currao, Condition Assessment of Bridge Decks through Ground-Penetrating Radar in Bridge Management Systems, J. Perform. Constr. Facil. 34 (2020) 1–13. https://doi.org/10.1061/(asce)cf.1943-5509.0001507.

[129] Z.W. Wang, M. Zhou, G.G. Slabaugh, J. Zhai, T. Fang, Automatic detection of bridge deck condition from ground penetrating radar images, IEEE Trans. Autom. Sci. Eng. 8 (2011) 633–640. https://doi.org/10.1109/TASE.2010.2092428.

[130] X. Ma, H. Liu, M.L. Wang, R. Birken, Automatic detection of steel rebar in bridge decks from ground penetrating radar data, J. Appl. Geophys. 158 (2018) 93–102. https://doi.org/10.1016/j.jappgeo.2018.07.010.

[131] K. Dinh, N. Gucunski, T.H. Duong, Migration-based automated rebar picking for condition assessment of concrete bridge decks with ground penetrating radar, NDT E Int. 98 (2018) 45–54. https://doi.org/10.1016/j.ndteint.2018.04.009.

[132] Z. Xiang, G. Ou, A. Rashidi, Robust cascaded frequency filters to recognize rebar in GPR data with complex signal interference, Autom. Constr. 124 (2021). https://doi.org/10.1016/j.autcon.2021.103593.

[133] Y. Wang, G. Cui, J. Xu, Semi-automatic detection of buried rebar in GPR data using a genetic algorithm, Autom. Constr. 114 (2020) 103186. https://doi.org/10.1016/j.autcon.2020.103186.

[134] P. Asadi, M. Gindy, M. Alvarez, A Machine Learning Based Approach for Automatic Rebar Detection and Quantification of Deterioration in Concrete Bridge Deck Ground Penetrating Radar B-scan Images, KSCE J. Civ. Eng. (2019) 1–10. https://doi.org/10.1007/s12205-019-2012-z.

[135] P. Asadi, M. Gindy, M. Alvarez, A. Asadi, A computer vision based rebar detection chain for automatic processing of concrete bridge deck GPR data, Autom. Constr. 112 (2020) 103106. https://doi.org/10.1016/j.autcon.2020.103106.

[136] P. Kaur, K.J. Dana, F.A. Romero, N. Gucunski, Automated GPR Rebar Analysis for Robotic Bridge Deck Evaluation, IEEE Trans. Cybern. 46 (2016) 2265–2276. https://doi.org/10.1109/TCYB.2015.2474747.

[137] K. Dinh, N. Gucunski, T.H. Duong, An algorithm for automatic localization and detection of rebars from GPR data of concrete bridge decks, Autom. Constr. 89 (2018) 292–298. https://doi.org/10.1016/j.autcon.2018.02.017.

[138] H. Ahmed, C.P. Le, H.M. La, Pixel-level classification for bridge deck rebar detection and localization using multi-stage deep encoder-decoder network, Dev. Built Environ. 14 (2023) 100132. https://doi.org/10.1016/j.dibe.2023.100132.

[139] H. Ahmed, H.M. La, N. Gucunski, Review of Non-Destructive Civil Infrastructure Evaluation for Bridges: State-of-the-Art Robotic Platforms, Sensors and Algorithms, Sensors. 20 (2020) 1–38. https://doi.org/https://doi.org/10.3390/s20143954.

[140] F. Hou, W. Lei, S. Li, J. Xi, M. Xu, J. Luo, Improved Mask R-CNN with distance guided intersection over union for GPR signature detection and segmentation, Autom. Constr.

121 (2021) 103414. https://doi.org/10.1016/j.autcon.2020.103414.

[141] W. Lei, J. Luo, F. Hou, L. Xu, R. Wang, X. Jiang, Underground cylindrical objects detection and diameter identification in GPR B-scans via the CNN-LSTM framework, Electron. 9 (2020) 1–16. https://doi.org/10.3390/electronics9111804.

[142] Y. Zheng, S. Wang, P. Zhang, T. Xu, J. Zhuo, Application of Nondestructive Testing Technology in Quality Evaluation of Plain Concrete and RC Structures in Bridge Engineering: A Review, Buildings. 12 (2022). https://doi.org/10.3390/buildings12060843.

[143] X. Xiong, Y. Tan, Deep learning-based detection of tie bars in concrete pavement using ground penetrating radar, Int. J. Pavement Eng. (2022). https://doi.org/10.1080/10298436.2022.2155648.

[144] Y. Yue, H. Liu, X. Meng, Y. Li, Y. Du, Generation of high-precision ground penetrating radar images using improved least square generative adversarial networks, Remote Sens. 13 (2021). https://doi.org/10.3390/rs13224590.

[145] S. Park, J. Kim, K. Jeon, J. Kim, S. Park, Improvement of gpr-based rebar diameter estimation using yolo-v3, Remote Sens. 13 (2021). https://doi.org/10.3390/rs13102011.

[146] H. Ahmed, H.M. La, K. Tran, Rebar detection and localization for bridge deck inspection and evaluation using deep residual networks, Autom. Constr. 120 (2020) 103393. https://doi.org/10.1016/j.autcon.2020.103393.

[147] M. Marzouk, E.M. Abdelkader, T. Zayed, A probabilistic-based deterioration model using Ground Penetrating Radar, ISARC 2018 - 35th Int. Symp. Autom. Robot. Constr. Int. AEC/FM Hackathon Futur. Build. Things. (2018). https://doi.org/10.22260/isarc2018/0136.

[148] M. Alsharqawi, T. Zayed, S. Abu Dabous, Integrated condition rating and forecasting method for bridge decks using Visual Inspection and Ground Penetrating Radar, Autom. Constr. 89 (2018) 135–145. https://doi.org/10.1016/j.autcon.2018.01.016.

[149] J. Kim, N. Gucunski, K. Dinh, Deterioration and Predictive Condition Modeling of Concrete Bridge Decks Based on Data from Periodic NDE Surveys, J. Infrastruct. Syst. 25 (2019) 1–12. https://doi.org/10.1061/(asce)is.1943-555x.0000483.

Appendix:

Table A1: Keywords composing the different clusters.

Cluster 1	Cluster 2	Cluster 3	Cluster 4
Bridge decks	Bars (metal)	Algorithms	Antennas
Civil infrastructure	Concrete buildings	Automatic detection	Chloride contamination
Concrete	Concrete construction	Automation	Chlorine compounds
Concrete bridge decks	Concrete cover	Bridge inspection	Concrete beams and girders
Concrete deterioration	Concrete slabs	Concrete inspection	Data handling
Concrete structures	Concrete testing	Convolutional neural network	Data processing
Condition assessment	Finite difference time domain method	Decision making	Electrochemical corrosion
Correlation coefficient	Ground penetrating radar	Deep learning	Microwave antennas
Data acquisition	Hyperbolas	Deep neural networks	Moisture
Defects	Numerical methods	Electromagnetic waves	Signal processing
Delamination	Permittivity	Image processing	Steel bars corrosion
Deterioration	Polarization	Learning systems	Structural health monitoring
Half-cell potential	Radar antennas	Machine learning	Surveys
Inspection	Rebar diameter	Neural networks	Transportation
Inverse problems	Reinforced concrete	Object detection	
K-means clustering	Reinforcing bars	Radar imaging	
Non-destructive testing	Steel	Rebar recognition	
Radar measurement	Time domain analysis	Robotics	
Reflection amplitude	Water content		
Travel time	Wave propagation		